American Journal of Water Science and Engineering
2026, Vol. 12, No. 2, pp. 39–63
https://doi.org/10.11648/j.ajwse.20261202.12

Research Article

Estimating Reference Evapotranspiration over Georgetown, Guyana, Using an Artificial Neural Network: A Comparative Analysis with 32 Empirical Methods

Bunnel Bernard*, **Dwayne Shorlon Renville**, **Linda Francois**

Department of Mathematics, Physics and Statistics, University of Guyana, Georgetown, Guyana

Abstract

This study investigates the capability of an Artificial Neural Network (ANN) model to estimate daily ETo using several meteorological variables in a data-limited region along Guyana's coast. The ANN was trained on historical data from 2001–2018 and independently evaluated over 2019–2022, with ETo computed by the FAO Penman–Monteith (PM-56) method serving as the reference benchmark. Model performance was assessed using standard statistical indicators, including the root mean square error (RMSE), mean absolute error (MAE), coefficient of determination (R^2), Nash–Sutcliffe efficiency (NSE), and index of agreement (IoA). In addition, the ANN model was compared against 32 commonly used empirical ETo estimation methods, encompassing temperature-based, radiation-based, and mass transfer-based approaches. Results indicate that the ANN reproduced PM-56 ETo estimates with high accuracy and minimal bias, achieving R^2 and NSE values exceeding 0.99 across the validation period. The ANN model also consistently outperformed all empirical methods across all performance metrics, demonstrating superior accuracy and robustness. Among conventional methods, the Hargreaves–Samani and Makkink approaches showed comparatively better performance, while mass transfer-based methods exhibited substantial deviations and poorer performance. These findings suggest that ANN-based models can serve as reliable alternatives for daily ETo estimation in regions where complete meteorological inputs for physically based methods are limited, thereby supporting improved water-resource and agricultural decision-making in Guyana and similar environments.

Keywords

Reference Evapotranspiration, Artificial Neural Network, Performance Metrics, Georgetown, Penman-Monteith, Model Validation

1. Introduction

Reference evapotranspiration (ETo) is a critical variable in hydrology, irrigation scheduling, and agricultural water management, as it represents the atmospheric demand for water through combined evaporation and plant transpiration processes [1]. Accurate estimation of ETo underpins efficient irrigation planning, drought management, and sustainable agricultural production, particularly in tropical regions where climatic variability directly influences water availability. In Guyana, a low-lying coastal country with a humid tropical climate and strong seasonal rainfall patterns, reliable ETo estimation is especially important

*Correspondence: Bunnel Bernard (Bunnel.barnard@uog.edu.gy)

Received: 25 April 2026; **Accepted:** 8 May 2026; **Published:** 18 May 2026

for optimising water use during dry periods and supporting climate-resilient agricultural systems.

The Food and Agriculture Organisation (FAO) Penman–Monteith (PM) equation is widely regarded as the standard method for estimating reference evapotranspiration due to its strong physical basis and demonstrated reliability across diverse climatic conditions [2-6]. By integrating both thermodynamic and aerodynamic components, the PM method generally outperforms simpler empirical approaches and is recommended for daily ETo estimation [7]. Despite these strengths, routine application of the PM method can be constrained by its dependence on multiple meteorological variables, including wind speed, solar radiation, humidity, and temperature, which may be inconsistently measured or subject to data quality limitations in many developing regions [8].

To address these practical constraints, data-driven techniques such as artificial neural networks (ANNs) have gained increasing attention for ETo estimation. ANNs are capable of capturing complex nonlinear relationships among meteorological variables without explicitly defining physical processes, making them attractive as computational alternatives to physically based models. Numerous studies have demonstrated the effectiveness of ANN-based approaches for ETo estimation under a wide range of climatic conditions [9-12]. However, most existing applications have focused on temperate, semi-arid, or Mediterranean climates, with comparatively limited evidence from humid tropical coastal environments.

In particular, the performance of ANN models for estimating ETo in Guyana has not been systematically evaluated. Given the country's distinctive climatic characteristics and its reliance on climate-sensitive agricultural systems, assessing whether ANN models can reliably reproduce FAO PM-based ETo estimates is of both scientific and practical importance. This study therefore applies an ANN model to estimate daily reference evapotranspiration for Georgetown, Guyana, using long-term meteorological observations from 2001 to 2022. The ANN is trained using historical data and evaluated against FAO Penman–Monteith ETo estimates over an independent validation period to assess its predictive accuracy and generalization capability. Additionally, The ANN model is also compared to 31 simple methods for estimation ETo, to assess its overall performance. This assessment is done using several performance metrics, name the; Root Mean Square Error (RMSE), Mean Absolute Error (MAE), Mean Bias Error (MBE), Mean Absolute Percentage Error (MAPE), Normalized Root Mean Square Error (NRMSE), Nash-Sutcliffe Efficiency (NSE), Coefficient of Determination (R^2) and Index of Agreement (IoA). This study contributes to the growing body of evidence on data-driven ETo estimation and provides insight into the suitability of ANN models as practical tools for evapotranspiration assessment in humid tropical coastal regions.

2. Materials and Methods

2.1. Study Location

Georgetown is located on the northern Atlantic coast of Guyana at approximately 6.80 °N latitude and 58.16 °W longitude, near the mouth of the Demerara River. The city lies at or slightly below sea level and represents a low-lying coastal environment strongly influenced by maritime conditions. Georgetown experiences a humid tropical rainforest climate, characterised by persistently high humidity, relatively uniform temperatures throughout the year, and pronounced seasonal rainfall variability driven by the migration of the Intertropical Convergence Zone (ITCZ).

Mean annual precipitation in Georgetown is approximately 2,339 mm, with rainfall distributed across two distinct wet seasons: a primary wet season from mid-April to early July and a secondary wet season from November to January [13]. Air temperatures remain consistently warm, with daytime maxima typically ranging between 30 ℃ and 34 ℃ and nighttime minima between 23 ℃ and 26 ℃. Relative humidity generally ranges from 75% to 80%, while coastal trade winds contribute to moderate but variable wind speeds.

These climatic characteristics: high humidity, limited temperature variability, seasonal rainfall concentration, and coastal wind influence, create a complex evapotranspiration regime that differs from arid or temperate regions where many ETo models have been developed and tested. As a result, Georgetown provides a relevant case study for evaluating the performance of data-driven models, such as artificial neural networks, for reference evapotranspiration estimation under humid tropical coastal conditions.

2.2. Weather Station, Data Source and Preprocessing

Daily meteorological data used in this study were obtained from the Hydrometeorological Service of Guyana (Hydromet), the national authority responsible for meteorological observations and hydrological monitoring in Guyana. Data were recorded at a synoptic weather station in Georgetown, located along the northern Atlantic coast at an elevation of approximately −1 m relative to mean sea level. The station operates in accordance with standard meteorological observation practices and provides long-term, continuous climate records representative of coastal urban conditions.

The dataset spans the period from 2001 to 2022 and consists of daily observations of maximum and minimum air temperature, average dew point temperature, and wind speed measured at a height of 2 m above ground level. These variables constitute the primary meteorological inputs for reference evapotranspiration estimation. Additional parameters required for the FAO Penman–Monteith method, including vapour pressure and solar radiation, were derived following the procedures outlined in [14].

Daily extraterrestrial radiation was computed as an intermediate step in estimating incoming solar radiation using the *sirad* package in R (version 4.5.1), which calculates radiation based on the Julian day and site latitude [15]. A latitude of 6.803 °N was used and converted to radians as required by the model formulation. Atmospheric pressure corrections were applied using the station elevation, consistent with FAO-56 recommendations.

Approximately 1% of the daily observations contained missing values. These gaps were filled using a k-nearest neighbour (KNN) imputation approach with $k = 5$, which preserves the multivariate structure of the dataset and is commonly applied in climatological and hydrological time-series preprocessing. The proportion of missing data was sufficiently small that imputation was not expected to affect model training or validation outcomes materially.

2.3. Estimation of Evapotranspiration Computation

The Penman-Monteith (PM) method was employed in this study to estimate reference evapotranspiration in accordance with FAO guidelines [14]. This method integrates principles of energy balance and aerodynamic processes and was implemented on a daily time scale. The equation is given as:

$$ETo = \frac{0.408 \cdot \Delta \cdot (R_n - G) + \gamma \cdot \frac{900}{T+273} \cdot u_2 \cdot (e_s - e_a)}{\Delta + \gamma \cdot (1 + 0.34 \cdot u_2)} \quad (1)$$

where:

Δ - slope of the vapour pressure curve (kPa/ ℃)
R_n - net radiation (MJ/m^2/day)
G - soil heat flux density (MJ/m^2/day)
γ - psychrometric constant (kPa/ ℃)
T - mean daily air temperature (℃)
u_2 - wind speed at 2 meters above ground (m/s)
e_s - saturation vapour pressure (kPa)
e_a - actual vapour pressure (kPa)

2.4. Formulas Used for Estimating Required Radiation and Vapour Pressure

A set of equations for the calculation of PM-ETO according to available weather data and the time step required was proposed by [14]. For the computation of daily ETO, the value of the G in the PM-ETO formula can be treated as zero.

Solar and net radiation

The following equation, proposed by [16], is used to approximate solar radiation,R_s from available weather data.

$$R_s = K_{Rs}\sqrt{(T_{max} - T_{min})} \cdot R_a \quad (2)$$

where k_{Rs} is set at 0.19 (for coastal regions) and R_a = Extraterrestrial radiation was calculated using the R sirad package in $Mj/m^2/day$

As outlined by [14], clear sky radiation can be estimated as follows:

$$R_{so} = (a_s + b_s) \cdot R_a \quad (3)$$

When calibrated values for a_s and b_S are not available, the following equation can be used for estimating clear sky radiation:

$$R_{so} = (0.75 + 2(10^{-}5) \cdot z) \cdot R_a \quad (4)$$

where Z is the elevation of the weather station in meters.

Net radiation is computed from the difference between the net short and long wave radiation:

$$R_n = R_{ns} - R_{nl} \quad (5)$$

$$R_{ns} = (1 - \alpha) \cdot R_s$$

where Rs and R_{ns} are solar and shortwave radiation ($Mj/m^2/day$) and α is the albedo of the reference crop ($\alpha = 0.23$), and

$$R_{\mathrm{nl}} = \sigma\left[\frac{T_{\mathrm{max,K}}^4 + T_{\mathrm{min,K}}^4}{2}\right](0.34 - 0.14\sqrt{e_{\mathrm{a}}}) \times \left(1.35\frac{R_{\mathrm{s}}}{R_{\mathrm{so}}} - 0.35\right) \quad (6)$$

Where R_{nl} is the net long-wave radiation ($MJ/m^2/day$), R_{so} is the clear sky solar radiation ($MJ/m^2/day$),$T_{max,k}$ and $T_{min,k}$ are the maximum and minimum air temperature in Kelvins (K), e_a= actual vapour pressure (kPa) and σ= Stefan-Boltzmann constant for a day

$$(4.93\text{x } 10^{-9} MJK^{-4}m^{-2}day^{-1}).$$

Mean Vapour pressure and vapour pressure

The following equation is used to approximate the daily actual vapour pressure, e_a [14]:

$$\mathrm{e_a} = \mathrm{e^{\circ}(T_{dew})} = 0.6108\exp\left[\frac{17.27\ \mathrm{T_{dew}}}{T_{\mathrm{dew}} + 237.3}\right] \quad (7)$$

Where e_a is the actual vapour pressure (kPa) and T_{dew} is the Dew point temperature (C°).

Mean saturation vapour pressure can be estimated using the following formula [14]:

$$\mathrm{e_s} = \frac{\mathrm{e^{\circ}(T_{max})} + \mathrm{e^{\circ}(T_{min})}}{2} \quad (8)$$

Where e_s is the mean saturation vapour pressure (kPa), T_{max}= Maximum air temperature and T_{min}= minimum air temperature.

Psychrometric constant

The psychrometric constant, γ, is given by the following equation [14]:

$$\gamma = \frac{c_p P}{\varepsilon \lambda} = 0.665 \times 10^{-3} P$$

where γ is the psychrometric constant $[\mathrm{kPa°C^{-1}}]$, P is the atmospheric pressure [KPa], λ is the latent heat of vaporisation, $2.45[\mathrm{MJkg^{-1}}]$, C_p is the specific heat at constant pressure, $(1.01310^{-3}[\mathrm{MJkg^{-1}°C^{-1}}])$ ε is the ratio of the molecular weight of water vapour/dry air $= 0.622$.

$$P = 101.3\left(\frac{293 - 0.0065z}{293}\right)^{5.26} \quad (9)$$

The slope of the saturation vapour pressure curve

According to the standards set out by [14], the slope of the saturation vapour curve can be calculated as follows:

$$\Delta = \frac{409\left[0.6108\exp\left(\frac{17.27T}{T+237.3}\right)\right]}{(T+237.3)^2} \quad (10)$$

2.5. ETo Estimates Using Empirical Methods

In this research, 32 simple methods for estimating ETo were tested to assess the performance of the ANN model on observed data. These methods were classified as temperature-based, radiation-based and mass-transfer based, depending on the input variables required. The table below shows the equation for each method used.

Table 1. *Empirical methods for estimating ETO (Celestin et al., 2020).*

No	Authors/ Models	Abbreviation	Methods/Formulation
Combination-based methods			
(1)	Penman-Monteith	FAO56	$ET_0 = \frac{0.408\Delta(Rn-G)+\gamma[900/(T_{mean}+273)]u_2(e_s-e_a)}{\Delta+\gamma(1+0.34u_2)}$
Temperature-based methods			
(2)	[16]	H-S	$ET_0 = [0.0023 \times Ra(T_{mean} + 17.8)(T_{max} - T_{min})^{0.5}]/\lambda$
(3)	[17]	TRAJ	$ET_0 = [0.0023 \times Ra(T_{mean} + 17.8)(T_{max} - T_{min})^{0.424}]/\lambda$
(4)	[18]	TAB1	$ET_0 = [0.0031 \times Ra(T_{mean} + 17.8)(T_{max} - T_{min})^{0.5}]/\lambda$
(5)	[18]	TAB2	$ET_0 = [0.0028 \times Ra(T_{mean} + 17.8)(T_{max} - T_{min})^{0.5}/\lambda]$
(6)	[19]	DAL1	$ET_0 = [0.003 \times Ra(T_{mean} + 20)(T_{max} - T_{min})^{0.4}]/\lambda$
(7)	[19]	DAL2	$ET_0 = [0.0025 \times Ra(T_{mean} + 16.8)(T_{max} - T_{min})^{0.5}]/\lambda$
(8)	[20]	BERT	$ET_0 = [0.00193 \times Ra(T_{mean} + 17.8)(T_{max} - T_{min})^{0.517}]/\lambda$
(9)	[21]	DORJ	$ET_0 = [0.002 \times Ra(T_{mean} + 33.9)(T_{max} - T_{min})^{0.296}]/\lambda$
(10)	[22]	BRO	$ET_0 = 0.109 \times (Ra/\lambda) + 0.157T_{max} + 0.158(T_{max} - T_{min}) - 5.39$
(11)	[23]	AHO1	$ET_0 = 0.252(Ra/\lambda) + 0.221T_{mean}(1 - RH_{mean}/100)$
(12)	[23]	AHO2	$ET_0 = 0.29(Ra/\lambda) + 0.15T_{max}(1 - RH_{mean}/100)$
Solar radiation- based methods			
(13)	[24]	MAK	$ET_0 = 0.7 \times (Rs/\lambda) \times [\Delta/\Delta + \gamma] - 0.12$
(14)	[25]	P-T	$ET_0 = 1.26(Rn - G)[\Delta/\Delta + \gamma]/\lambda$
(15)	[26]	JENH	$ET_0 = (0.025T_{mean} + 0.08)Rs/\lambda$
(16)	[27]	HARG	$ET_0 = [0.0135(T_{mean} + 17.8)Rs]/\lambda$
(17)	[28]	ABT1	$ET_0 = 0.52T_{max}Rs/\lambda$
(18)	[28]	ABT2	$ET_0 = (T_{max}/56) \times (Rs/\lambda)$
(19)	[29]	IRM1	$ET_0 = -0.611 + 0.149Rs + 0.079T_{mean}$
(20)	[29]	IRM2	$ET_0 = 0.469 + 0.289Rn + 0.023T_{mean}$
(21)	[18]	TAB3	$ET_0 = -0.642 + 0.174Rs + 0.0353T_{mean}$
(22)	[18]	TAB4	$ET_0 = -0.478 + 0.156Rs - 0.0112T_{max} + 0.0733T_{min}$
(23)	[30]	OUD	$ET_0 = (Rs/\lambda) \times [T_{mean} + 5]/100$

No	Authors/ Models	Abbreviation	Methods/Formulation
(24)	[31]	DALT	$ET_0 = (3.648 + 0.7223u_2)(e_s - e_a)$
(25)	[32]	MEY	$ET_0 = (3.75 + 0.503u_2)(e_s - e_a)$
(26)	[33]	ROH	$ET_0 = (3.3 + 0.891u_2)(e_s - e_a)$
(27)	[34]	ALB	$ET_0 = (1.005 + 2.97u_2)(e_s - e_a)$
(28)	[35]	WMO	$ET_0 = (1.298 + 0.934u_2)(e_s - e_a)$
(29)	[36]	TRAB	$ET_0 = 0.3075 \times u_2{}^{0.5}(e_s - e_a)$
(30)	[37]	BRWE	$ET_0 = 0.543 \times u_2{}^{0.456}(e_s - e_a)$
(31)	[38]	MAHR	$ET_0 = 0.286 \times u_2{}^{0.5}(e_s - e_a)$
(32)	[39]	PENM	$ET_0 = (2.625 + 0.000479u_2)(e_s - e_a)$
(33)	[40]	ROM	$ET_0 = 0.00006(100 - RH_{mean})(25 + T_{mean})^2$

ET_0: reference crop evapotranspiration (mm day^{-1}); e_a: actual vapor pressure (kPa); e_s: saturation vapor pressure (kPa); $(e_s - e_a)$: saturation vapor pressure deficit (kPa); G: soil heat flux density (mm day^{-1}); n: actual duration of sunshine in a day (h); Ra: extraterrestrial radiation (mm day^{-1}); RH_{mean}: mean relative humidity (%); RH_{max}: maximum relative humidity (%); RH_{min}: minimum relative humidity (%); Rn: net solar radiation (MJ/m^2 day); Rs: solar radiation (MJ m^{-2} day^{-1}); T_{mean}: mean daily temperature (°C); u_2: wind speed measured at 2 m height (m s^{-1}); Δ: slope of saturation vapor pressure curve (mb °C^{-1}); γ: psychrometric constant, (kPa °C^{-1}); λ: latent heat of vaporization (MJ kg^{-1}).

2.6. Artificial Neural Networks

Artificial Neural Networks (ANNs) are computational models inspired by the structure and functioning of biological neural systems. They are capable of learning from data, identifying patterns, and adapting their responses through experience, which makes them highly effective for complex data analysis tasks [41]. Mathematically, ANNs act as nonlinear regression models that rely on weighted connections to map inputs to outputs.

A typical ANN consists of three main components: the input layer, one or more hidden layers, and the output layer. Each layer is made up of interconnected processing units, or neurons, with the strength of these connections determined by adjustable weights. The structure of an ANN is often denoted by a notation such as ANN(i–j–k), where i, j and k represent the number of neurons in the input, hidden, and output layers, respectively [12].

In the context of ETo estimation, the number of input neurons is determined by the number of climatic variables used, while the output layer typically contains a single neuron to produce the ETo estimate. For most evapotranspiration modelling applications, a single hidden layer is generally sufficient to achieve high predictive accuracy [9].

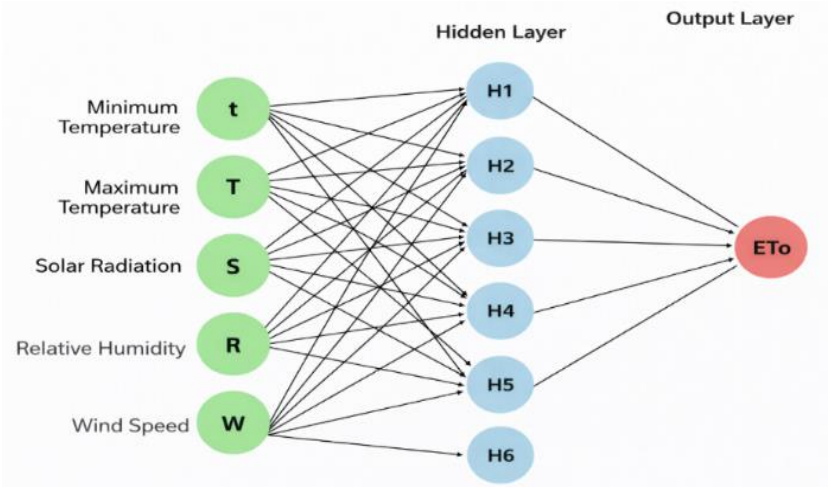

Figure 1. *(5-6-1) Structure of the artificial neural network.*

Architectural structure

To determine the architectural structure of our ANN model, we employed the method used by [42]. This method showed that an appropriate order for an ANN model can be obtained by using the formula $\frac{4n^2+3}{n^2-8}$, where n represents the number of input layers. Since this study uses five input values, n was set to 5. From this, the appropriate model structure was determined to be (5-6-1).

Learning algorithms

The learning algorithm plays a central role in optimising the objective function and largely determines the model's ability to learn effectively, provided that an adequate amount of data is available [43]. In this study, the Root Mean Square Propagation (RMSprop) algorithm is employed. RMSprop works by keeping a moving average of the recent squared gradients for each weight, which helps to adaptively adjust the learning rate during training [44].

The RMSprop algorithm is given by:

$$w_{\text{new}} = w_{\text{old}} - \frac{\alpha}{\sqrt{\text{MS}(w,t)}}\nabla E(w_{\text{old}}) \tag{11}$$

Where w_{new} and w_{old} are the new and old weights, α is the learning rate, which was set to 0.0001, ∇E is the gradient of the cost function, and $\text{MS}(w,t)$ is given by:

$$\begin{aligned}\text{MS}(w,t) = \quad & \gamma_d \text{MS}(w,t-1) \\ & +(1-\gamma_d)(\nabla E(w))^2\end{aligned} \tag{12}$$

and γ_d is the decay level in the rms term $= 0.9$; $t =$ the target output and $\text{MS} =$ mean square.

Activation function

The activation function plays a crucial role in artificial neural networks (ANNs), as it is responsible for converting the aggregated input signals into outputs that are passed to subsequent layers. This transformation typically involves applying a mathematical function to the weighted sum of the inputs, thereby determining the output of each neuron in the network.

In the context of evapotranspiration estimation, the sigmoid activation function has been commonly used, as seen in studies by [12, 43, 45, 46]. However, recent research has explored alternative activation functions with improved performance. For instance, [43] demonstrated that the Rectified Linear Unit (ReLU) outperformed the sigmoid function in both accuracy and computational efficiency. Similarly, Maqsood et al. (2022) found that ReLU delivered superior predictive capability compared to sigmoid in ETo modelling applications.

Based on these findings, this study adopts the ReLU activation function, defined as:

$$f(x) = \max(0, x) \tag{13}$$

Batch size and Epoch

The number of epochs refers to how many times the entire training dataset passes through the network during training. Too few epochs may result in underfitting, while too many can cause overfitting, similar to using too many hidden neurons [43]. The batch size, on the other hand, defines how many samples are processed at a time in each training step. Based on [43], this study used a small fixed batch size of 16 and trained the model over 500 epochs to promote sufficient learning and ensure convergence.

Standardisation, Loss Function, and Training/Testing

To enhance the training process, both input and output variables were standardised using the min-max normalisation method, transforming values into a dimensionless range between 0 and 1. This approach improves convergence speed and consistency during model training [12]. Model performance was evaluated using the mean squared error (MSE) loss function, which measures the average squared difference between observed and predicted ETo values. Minimising this error is central to the learning process.

Training was conducted using the mini-batch gradient descent algorithm, where small batches of data are processed iteratively to update model weights. A batch size of 10 was used. During training, the model learns by minimising error, while in the testing phase, the model's generalisation performance is assessed on unseen data [43]. The dataset was split into training and testing sets, with a train-test ratio of 81: 19.

2.7. Statistical Analysis of Model Performance

The accuracy and reliability of the artificial neural network (ANN) model in estimating reference evapotranspiration (ETo) were assessed using several statistical performance metrics. These included:

1) Root Mean Square Error (RMSE)
2) Mean Absolute Error (MAE)
3) Mean Bias Error (MBE)
4) Mean Absolute Percentage Error (MAPE)
5) Normalised Root Mean Square Error (NRMSE)
6) Nash-Sutcliffe Efficiency (NSE)
7) Coefficient of Determination (R^2)
8) Index of Agreement (IoA)

These metrics provide a comprehensive evaluation of model accuracy, bias, and consistency. Definitions for each metric are as follows:

RMSE measures the square root of the average squared differences between predicted and observed ETo values, emphasising larger errors.

$$\text{RMSE} = \sqrt{\frac{1}{N}\sum_{i=1}^{N}\left(ET_{\text{pred},i} - ET_{\text{obs},i}\right)^2} \tag{14}$$

MAE is the average absolute difference between predicted and observed values.

$$\text{MAE} = \frac{1}{N}\sum_{i=1}^{N}\left|ET_{\text{pred},i} - ET_{\text{obs},i}\right| \tag{15}$$

MBE indicates the average bias in the predictions.

$$\mathrm{MBE} = \frac{1}{N}\sum_{i=1}^{N}\left(ET_{\mathrm{pred},i} - ET_{\mathrm{obs},i}\right) \quad (16)$$

MAPE provides the average percentage error between predicted and observed values.

$$\mathrm{MAPE} = \frac{100}{N}\sum_{i=1}^{N}\left|\frac{ET_{\mathrm{pred},i} - ET_{\mathrm{obs},i}}{ET_{\mathrm{obs},i}}\right| \quad (17)$$

NRMSE normalises RMSE by the mean of observed values.

$$\mathrm{NRMSE} = \frac{\mathrm{RMSE}}{\overline{ET_{\mathrm{obs}}}} \times 100 \quad (18)$$

NSE evaluates the predictive power of the model relative to the mean of observed data.

$$\mathrm{NSE} = 1 - \frac{\sum_{i=1}^{N}\left(ET_{\mathrm{obs},i} - ET_{\mathrm{pred},i}\right)^2}{\sum_{i=1}^{N}\left(ET_{\mathrm{obs},i} - \overline{ET_{\mathrm{obs}}}\right)^2} \quad (19)$$

The Coefficient of Determination (R^2) quantifies the proportion of variance in the observed data explained by the model.

$$R^2 = \left[\frac{\sum_{i=1}^{N}\left(ET_{\mathrm{obs},i} - \overline{ET_{\mathrm{obs}}}\right)\left(ET_{\mathrm{pred},i} - \overline{ET_{\mathrm{pred}}}\right)}{\sqrt{\sum_{i=1}^{N}\left(ET_{\mathrm{obs},i} - \overline{ET_{\mathrm{obs}}}\right)^2 \sum_{i=1}^{N}\left(ET_{\mathrm{pred},i} - \overline{ET_{\mathrm{pred}}}\right)^2}}\right]^2 \quad (20)$$

IoA (Index of Agreement) measures how well the model predictions match the observations, ranging from 0 (no agreement) to 1 (perfect agreement).

$$\mathrm{IoA} = 1 - \frac{\sum_{i=1}^{N}\left(ET_{\mathrm{pred},i} - ET_{\mathrm{obs},i}\right)^2}{\sum_{i=1}^{N}\left(\left|ET_{\mathrm{pred},i} - \overline{ET_{\mathrm{obs}}}\right| + \left|ET_{\mathrm{obs},i} - \overline{ET_{\mathrm{obs}}}\right|\right)^2} \quad (21)$$

These metrics collectively offer insight into the ANN model's prediction accuracy, error distribution, directional bias, and capacity to capture the variability in observed ETo values.

3. Results

Table 2. *Descriptive measures of ANN input variables.*

Input	Min	Max	Mean	Std	Skewness		Kurtosis	
					Statistic	Std. Error	Statistic	Std. Error
MinTemp	20.8	26.8	24.252	0.869	-0.237	0.064	0.345	0.128
MaxTemp	24.6	34.9	31.503	1.445	-0.533	0.064	1.088	0.128
RelativeHum	57.446	97.216	75.226	5.69	0.231	0.064	0.53	0.128
SolarRad	6.53	20.1	15.33	1.84	-0.62	0.064	1.09	0.128
Windspeed	1.471	3.937	2.992	0.337	-0.467	0.064	0.646	0.128

Table 1 summarises the descriptive statistics of the meteorological variables used as inputs during the testing phase of the artificial neural network (ANN) model, based on weather data recorded from 2019 to 2022. The input variables include minimum temperature (MinTemp), maximum temperature (MaxTemp), relative humidity (RelativeHum), solar radiation (SolarRad), and wind speed (Windspeed). Overall, the statistics provide insight into the range, variability, and distributional characteristics of the predictors used for model evaluation.

Minimum temperature during the testing period ranged from 20.8 ℃ to 26.8 ℃, with a mean of 24.25 ℃ and a standard deviation of 0.87 ℃, indicating relatively low variability. The distribution exhibited slight negative skewness (-0.237) and low kurtosis (0.345), suggesting an approximately symmetric distribution. In contrast, maximum temperature showed greater variability, ranging from 24.6 ℃ to 34.9 ℃, with a mean of 31.50 ℃ and a standard deviation of 1.44 ℃. This variable displayed moderate negative skewness (-0.533) and positive kurtosis (1.088), indicating a mildly left-skewed and more peaked distribution.

Relative humidity values varied between 57.45% and 97.22%, with an average of 75.23% and a standard deviation of 5.69%. The distribution was slightly positively skewed (0.231) with modest kurtosis (0.530), reflecting mild tail heaviness. Solar radiation ranged from 6.53 MJ/m ²to 20.10 MJ/m ², with a mean of 15.33 MJ/m ²and a standard deviation of 1.84 MJ/m ². Its distribution showed moderate negative skewness (-0.620) and positive kurtosis (1.090), indicating a slightly left-skewed and more peaked distribution relative to normal.

Wind speed exhibited the smallest variability among the input variables, ranging from 1.47 m/s to 3.94 m/s, with a mean of 2.99 m/s and a standard deviation of 0.34 m/s. The distribution was slightly negatively skewed (-0.467) with low kurtosis (0.646), suggesting a near-normal distribution with limited extreme values.

In addition to the summary statistics, the temporal evolution of the input variables is illustrated in Figure 2 through time-series plots covering the 2019–2022 period. The plots highlight the day-to-day variability and seasonal fluctuations in minimum and maximum temperature, relative humidity, solar radiation, and wind speed, reflecting the expected meteorological dynamics of the study region. Maximum temperature and solar radiation exhibit pronounced seasonal patterns and notable short-term fluctuations, whereas relative humidity, minimum temperature, and wind speed display more gradual day-to-day changes, indicating comparatively smoother temporal variability. These time-series representations complement the descriptive statistics by visually confirming the stability, range, and temporal structure of the input variables used in the ANN model.

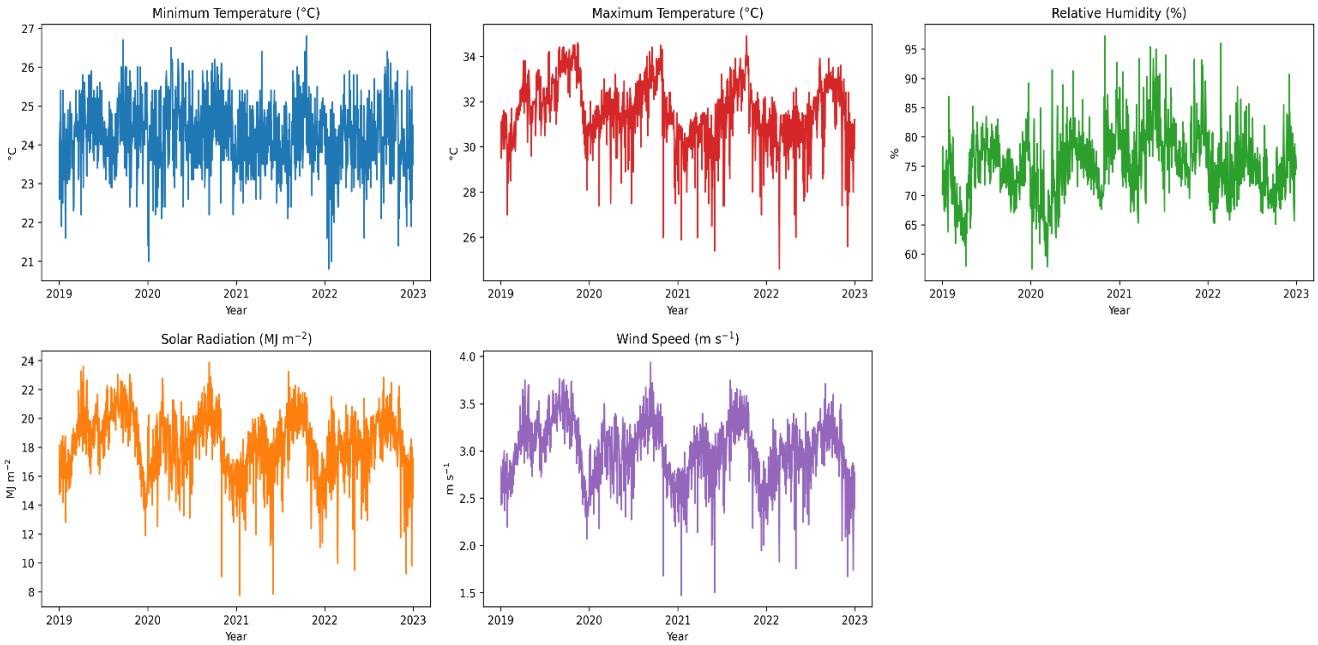

Figure 2. *Time series plot of ANN input variables from 2019-2022.*

3.1. Observed ETo Computed via Penman-Monteith

Table 3. *Summary statistics of observed ETo from 2019-2022.*

Min	Max	Mean	Std	Skewness		Kurtosis	
	Statistic	Statistic	Statistic	Statistic	Std. Error	Statistic	Std. Error
1.531	5.864	4.154	0.647	-. 514	. 064	. 587	. 128

In Table 2, the descriptive statistics of the observed daily reference evapotranspiration (ETo) values, calculated using the FAO Penman–Monteith method for the period 2019–2022, reveal key insights into the evaporative demand of the atmosphere in Georgetown, Guyana. The ETo values ranged from a minimum of 1.531 mm/day to a maximum of 5.864 mm/day, with a mean value of 4.154 mm/day and a standard deviation of 0.647 mm/day. This indicates moderate variability around the mean, suggesting relatively consistent daily atmospheric conditions with periodic fluctuations. The distribution of ETo was slightly negatively skewed (skewness =-0.514), indicating a greater frequency of lower ETo values compared to higher ones. Additionally, the kurtosis value of 0.587 implies a distribution that is marginally more peaked than the normal

distribution, suggesting the presence of a relatively sharp central peak with fewer extreme deviations. The temporal evolution of the observed daily ETo over the study period is illustrated in Figure 3, which highlights the seasonal variability and day-to-day fluctuations in atmospheric evaporative demand that are consistent with the statistical characteristics reported in Table 2. Overall, the ETo data reflect a stable evaporative pattern during the study period, with occasional variability driven by seasonal and meteorological changes.

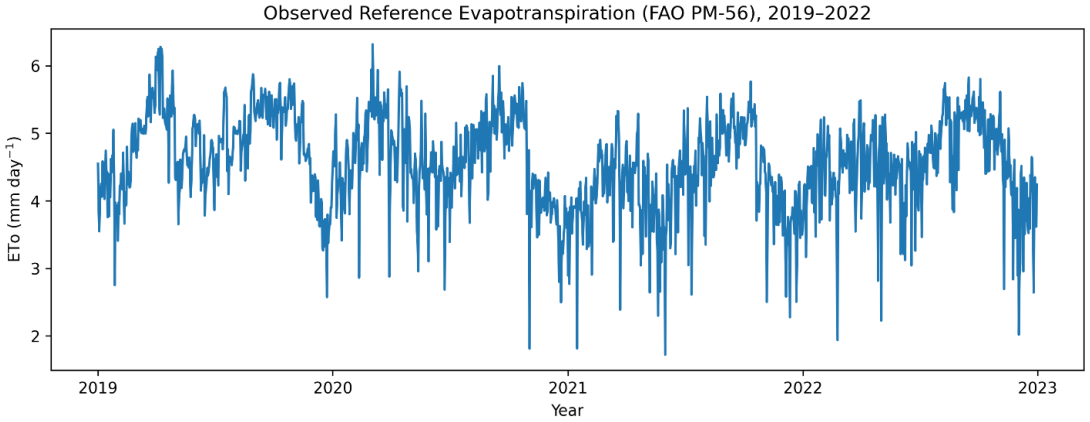

Figure 3. *Observed ETo from 2019-2022.*

3.2. Descriptive Measures of ETo Computed by ANN Model and Other Empirical Methods

Table 4. *Summary statistics of ETo estimated by ANN and other empirical methods from 2019-2022.*

Method	Min	Max	Mean	Std	Skewness	Kurtosis	Q1	Q3	Q10	Q80	Q99
FAO56	1.531	5.864	4.154	0.647	-0.514	3.581	3.771	4.639	3.335	4.739	5.433
HS	1.647	5.391	4.114	0.539	-0.578	3.902	3.778	4.507	3.435	4.571	5.146
TRAJ	1.597	4.488	3.539	0.416	-0.625	3.946	3.276	3.848	3.007	3.897	4.303
TAB1	2.219	7.266	5.545	0.727	-0.578	3.902	5.093	6.075	4.630	6.161	6.935
TAB2	2.005	6.563	5.009	0.656	-0.578	3.902	4.600	5.487	4.182	5.565	6.264
DAL1	2.168	5.792	4.613	0.519	-0.641	3.956	4.286	5.003	3.943	5.062	5.561
DAL2	1.748	5.731	4.374	0.574	-0.576	3.897	4.018	4.792	3.652	4.861	5.473
BERT	1.391	4.715	3.571	0.479	-0.566	3.885	3.272	3.921	2.967	3.976	4.494
DORJ	1.812	3.883	3.230	0.296	-0.697	3.873	3.035	3.451	2.833	3.489	3.749
BRO	0.397	3.365	2.293	0.457	-0.471	3.798	2.015	2.617	1.746	2.690	3.221
AHO1	3.708	6.659	5.210	0.441	-0.187	3.129	4.937	5.518	4.626	5.583	6.193
AHO2	4.152	6.608	5.410	0.384	-0.251	3.022	5.169	5.679	4.880	5.736	6.232
MAK	1.747	5.624	4.260	0.527	-0.621	4.082	3.930	4.640	3.595	4.718	5.297
PT	2.582	6.769	5.176	0.580	-0.480	3.548	4.793	5.591	4.421	5.695	6.340
JENH	1.885	6.394	4.871	0.666	-0.545	3.803	4.466	5.358	4.034	5.460	6.135
HARG	1.546	5.063	3.864	0.506	-0.578	3.902	3.548	4.233	3.226	4.293	4.832
ABT2	1.223	4.924	3.536	0.552	-0.399	3.541	3.184	3.935	2.847	4.012	4.650
IRM1	2.329	4.589	3.876	0.321	-0.699	4.303	3.682	4.110	3.479	4.157	4.469

Method	Min	Max	Mean	Std	Skewness	Kurtosis	Q1	Q3	Q10	Q80	Q99
IRM2	2.498	4.915	4.019	0.338	-0.504	3.609	3.801	4.266	3.578	4.315	4.688
TAB3	1.382	3.841	3.010	0.340	-0.663	4.196	2.796	3.254	2.585	3.298	3.668
TAB4	2.035	3.924	3.339	0.268	-0.741	4.276	3.169	3.541	3.001	3.568	3.813
OUD	0.803	2.702	2.061	0.280	-0.551	3.820	1.891	2.265	1.709	2.306	2.596
DALT	0.431	10.781	5.581	1.507	-0.214	3.166	4.612	6.666	3.741	6.945	8.777
MEY	0.407	9.690	5.044	1.344	-0.222	3.185	4.193	6.013	3.405	6.256	7.880
ROH	0.425	11.133	5.737	1.568	-0.206	3.147	4.730	6.859	3.823	7.150	9.023
ALB	0.531	19.079	9.561	2.839	-0.138	3.016	7.727	11.637	6.039	12.096	15.424
WMO	0.254	7.772	3.946	1.125	-0.173	3.081	3.222	4.763	2.574	4.934	6.291
TRAB	0.035	0.996	0.511	0.141	-0.205	3.142	0.422	0.612	0.340	0.637	0.806
BRWE	0.061	1.670	0.860	0.236	-0.210	3.154	0.709	1.028	0.573	1.072	1.354
MAHR	0.033	0.926	0.475	0.131	-0.205	3.142	0.392	0.569	0.316	0.593	0.750
PENM	0.233	4.739	2.513	0.644	-0.233	3.228	2.101	2.965	1.741	3.083	3.888
ROM	0.418	7.575	4.175	1.022	-0.251	3.337	3.522	4.892	2.954	5.072	6.366
ANN	1.154	5.762	4.159	0.648	-0.650	4.189	3.793	4.672	3.373	4.758	5.380

The descriptive statistics for all 33 methods are presented in Table 4, providing insights into the central tendency, dispersion, and distributional characteristics of daily ETo estimates from 2019 to 2022. The artificial neural network (ANN) model demonstrated exceptional agreement with observed ETo, producing nearly identical mean (4.159 mm day^{-1}) and standard deviation (0.648 mm day^{-1}) values. The range of ANN estimates ($1.154 - 5.762$ mm^{-1} day) and distributional characteristics (skewness = -0.650, kurtosis $= 4.189$) closely mirrored observed data, confirming that the ANN successfully captured both the magnitude and variability of reference evapotranspiration.

Among temperature-based methods, performance varied. The [16] method showed the closest agreement with observed data (mean $= 4.114$ mm day^{-1}), while the [18] formulations overestimated ETo (means of 5.545 and 5.009 mmday^{-1}). Conversely, the [22] method underestimated ETo (mean = 2.293 mm day^{-1}). Most temperature-based methods exhibited negative skewness (0.471 to -0.697) and kurtosis values between 3.1 and 4.0, similar to observed ETo.

Radiation-based methods showed mixed performance. The [24] method agreed well with observed ETO (mean = 4.260 mm day^{-1}), while the [25] approach moderately overestimated ETo (mean $= 5.176$ mm day^{-1}). The [30] formulation severely underestimated ETo (mean $= 2.061$ mm day^{-1}), representing the poorest performer in this category.

Mass transfer-based methods exhibited the greatest variability, with the [34] approach producing exceptionally high ETo values (mean = 9.561 mm day-1), while the [36, 38] methods severely underestimated ETo (means of 0.511 and 0.475 mm day^{-1}, respectively). These methods generally showed the lowest negative skewness (-0.138 to -0.251) and kurtosis values approaching 3, indicating near-normal distributions, though their extreme ranges highlight high sensitivity to wind-speed inputs.

Percentile analysis further confirmed the ANN's performance, with Q10 (3.373 mm day^{-1}), Q80 (4.758 mm day^{-1}), and Q99 (5.380 mmday^{-1}) values closely matching observed ETo values (3.335,4.739, and 5.433 mm day^{-1}, respectively). In contrast, mass transfer methods showed the widest percentile ranges, with Q99 values ranging from 0.750 mm day^{-1} (Mahringer) to 15.424 mm day^{-1} (Albrecht).

Overall, the ANN model demonstrated superior agreement with reference ETo across all descriptive measures, outperforming temperature-based, radiation-based, and mass transfer-based methods. Among traditional methods, the Hargreaves-Samani and Makkink methods showed the closest alignment with the observed values, while mass transfer methods exhibited the poorest performance, highlighting the limitations of aerodynamic approaches for ETo estimation in Guyana. The variability, distribution and statistical closeness of each method to observed ETo can be seen in Figures 3 (scatter plot), 4 (Density plot) and 5 (box plot).

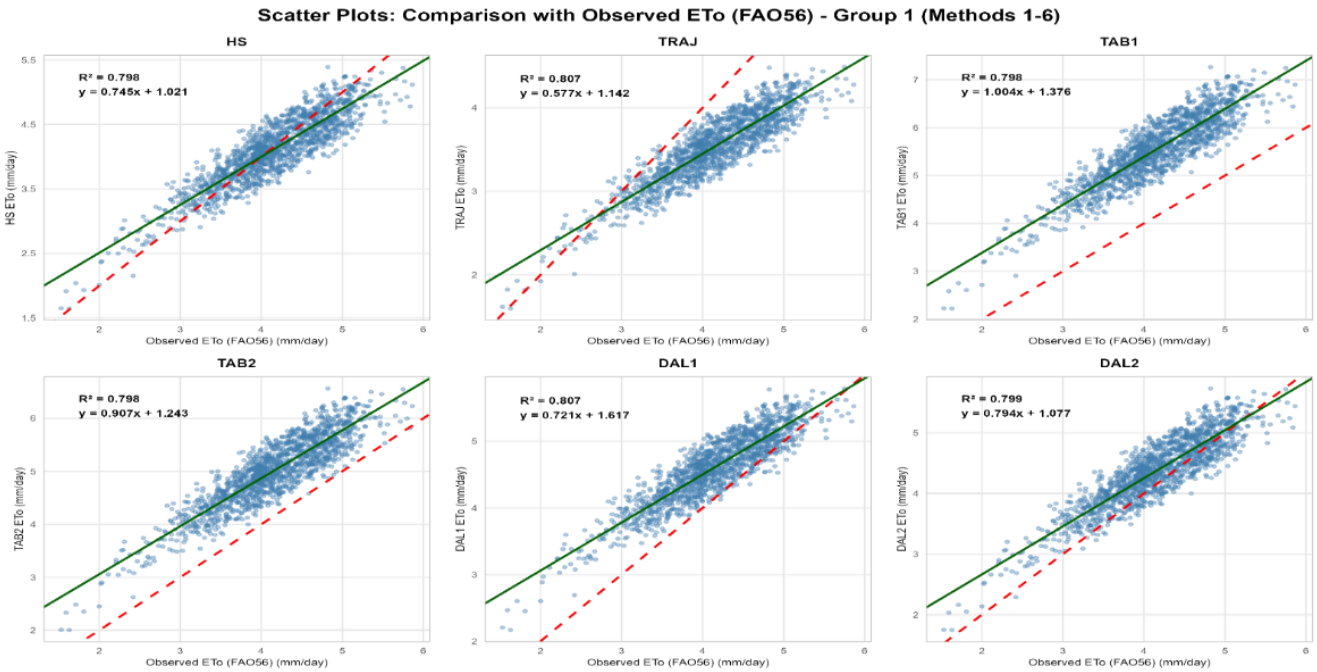
Scatter Plots: Comparison with Observed ETo (FAO56) - Group 1 (Methods 1-6)
HS
R² = 0.798
y = 0.745x + 1.021
TRAJ
R² = 0.807
y = 0.577x + 1.142
TAB1
R² = 0.798
y = 1.004x + 1.376
TAB2
R² = 0.798
y = 0.907x + 1.243
DAL1
R² = 0.807
y = 0.721x + 1.617
DAL2
R² = 0.799
y = 0.794x + 1.077
Observed ETo (FAO56) (mm/day)

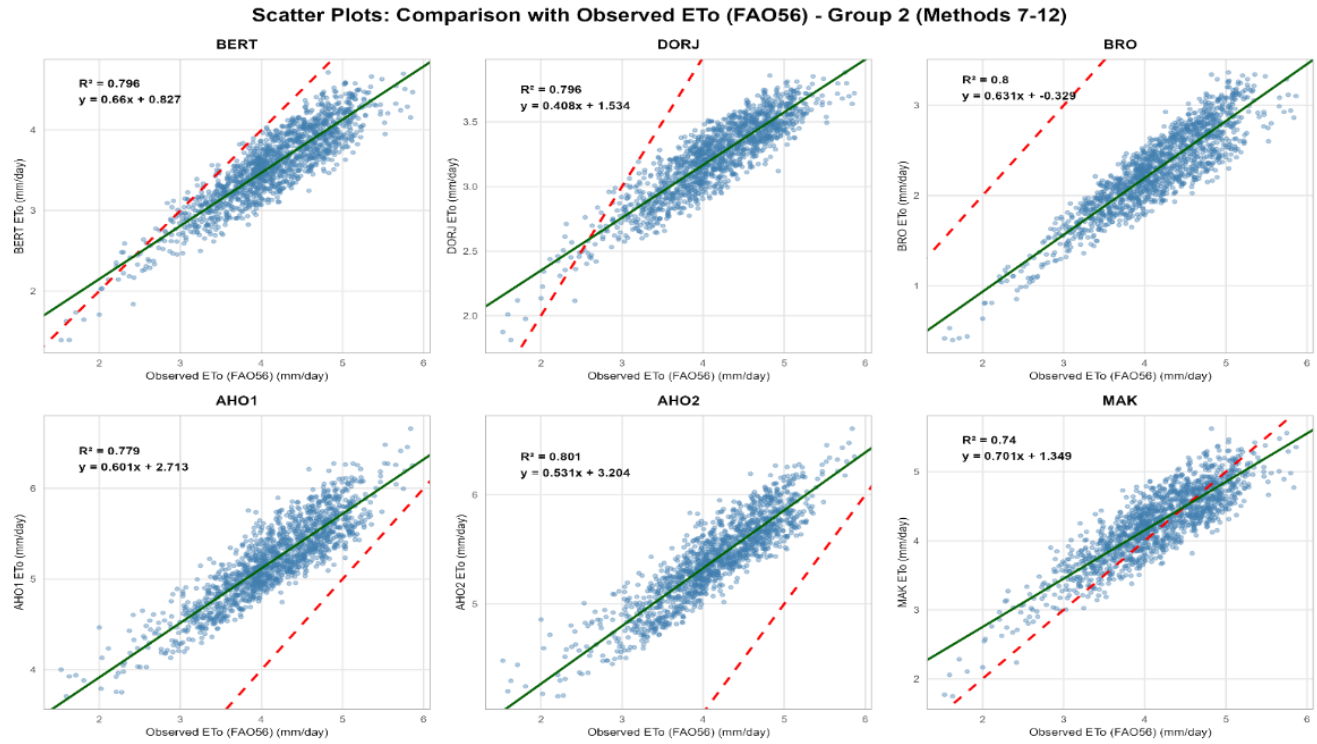
Scatter Plots: Comparison with Observed ETo (FAO56) - Group 2 (Methods 7-12)
BERT
R² = 0.796
y = 0.66x + 0.827
DORJ
R² = 0.796
y = 0.408x + 1.534
BRO
R² = 0.8
y = 0.631x + -0.329
AHO1
R² = 0.779
y = 0.601x + 2.713
AHO2
R² = 0.801
y = 0.531x + 3.204
MAK
R² = 0.74
y = 0.701x + 1.349
Observed ETo (FAO56) (mm/day)

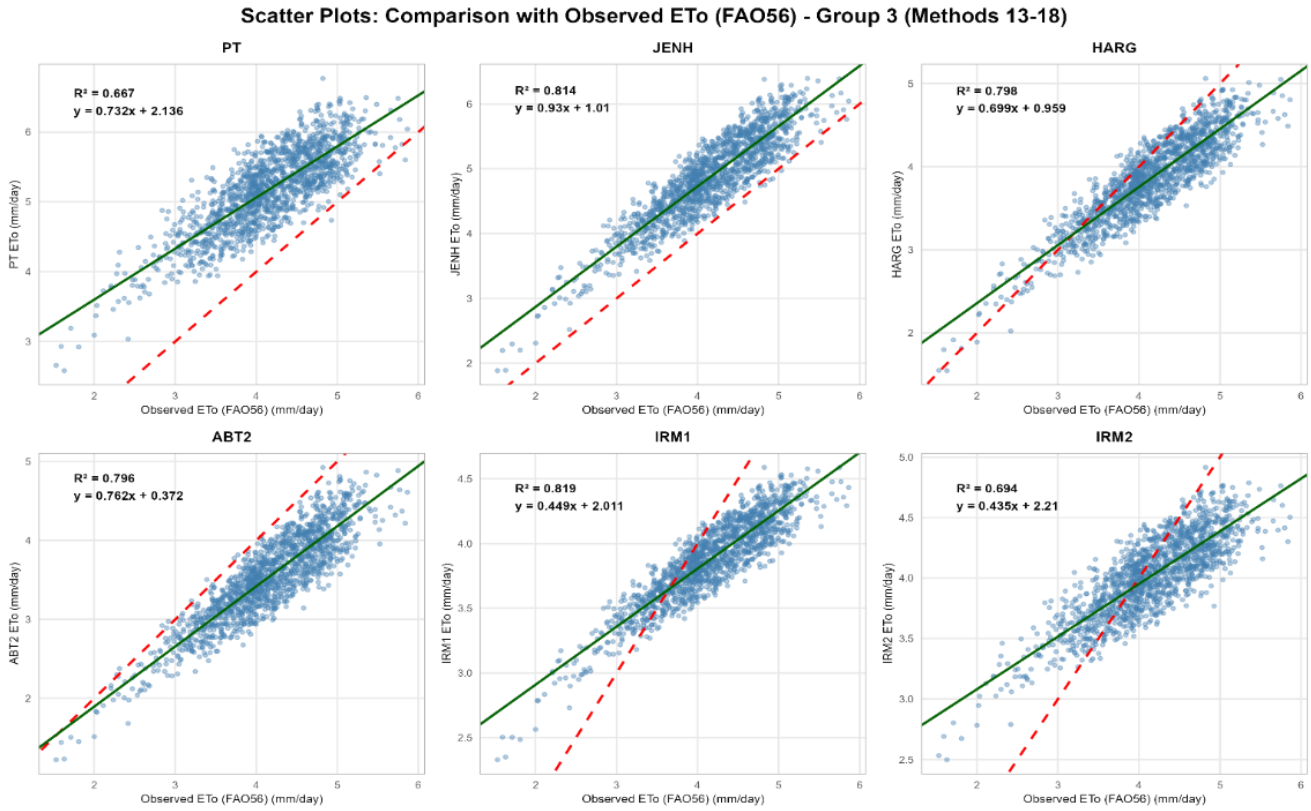
Scatter Plots: Comparison with Observed ETo (FAO56) - Group 3 (Methods 13-18)
PT
R² = 0.667
y = 0.732x + 2.136
PT ETo (mm/day)
JENH
R² = 0.814
y = 0.93x + 1.01
JENH ETo (mm/day)
HARG
R² = 0.798
y = 0.699x + 0.959
HARG ETo (mm/day)
ABT2
R² = 0.796
y = 0.762x + 0.372
ABT2 ETo (mm/day)
IRM1
R² = 0.819
y = 0.449x + 2.011
IRM1 ETo (mm/day)
IRM2
R² = 0.694
y = 0.435x + 2.21
IRM2 ETo (mm/day)
Observed ETo (FAO56) (mm/day)

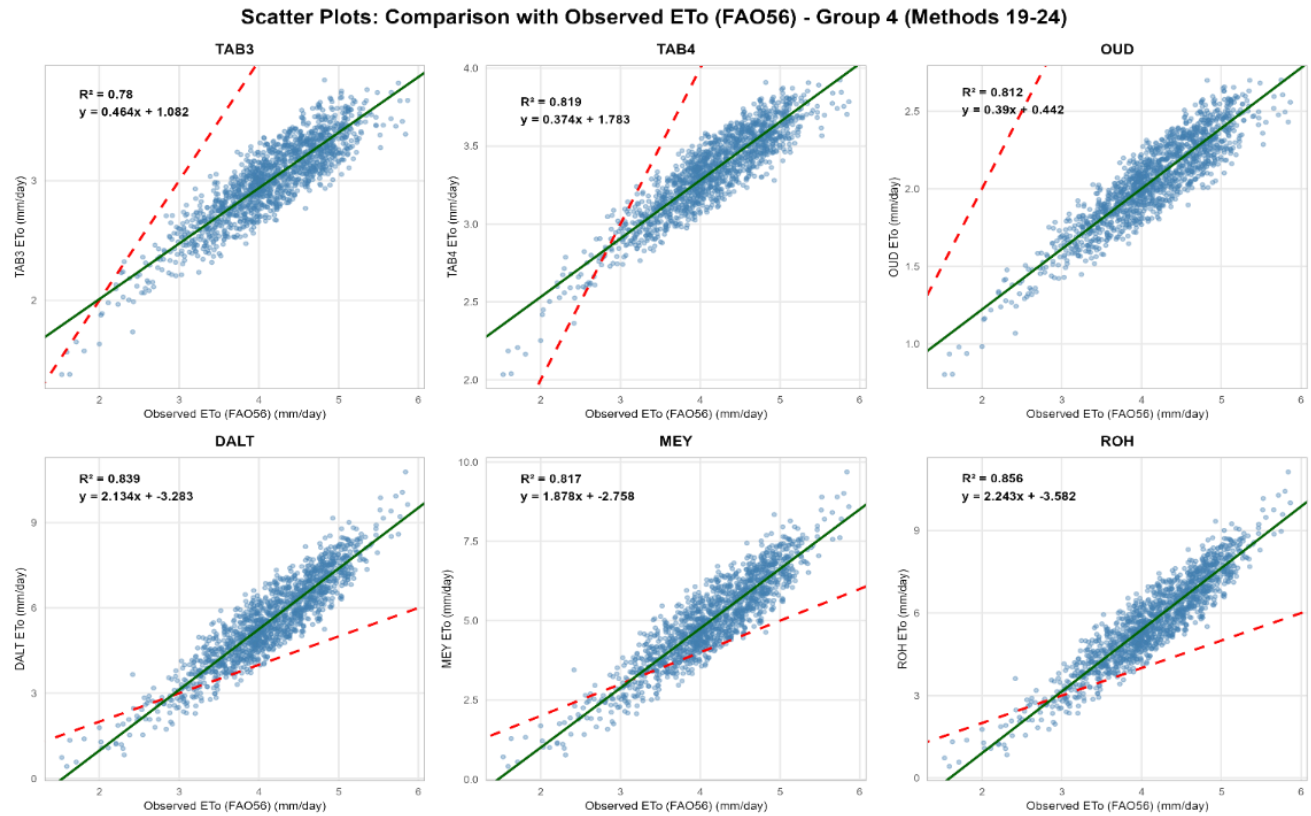
Scatter Plots: Comparison with Observed ETo (FAO56) - Group 4 (Methods 19-24)
TAB3
R² = 0.78
y = 0.464x + 1.082
TAB3 ETo (mm/day)
TAB4
R² = 0.819
y = 0.374x + 1.783
TAB4 ETo (mm/day)
OUD
R² = 0.812
y = 0.39x + 0.442
OUD ETo (mm/day)
DALT
R² = 0.839
y = 2.134x + -3.283
DALT ETo (mm/day)
MEY
R² = 0.817
y = 1.878x + -2.758
MEY ETo (mm/day)
ROH
R² = 0.856
y = 2.243x + -3.582
ROH ETo (mm/day)
Observed ETo (FAO56) (mm/day)

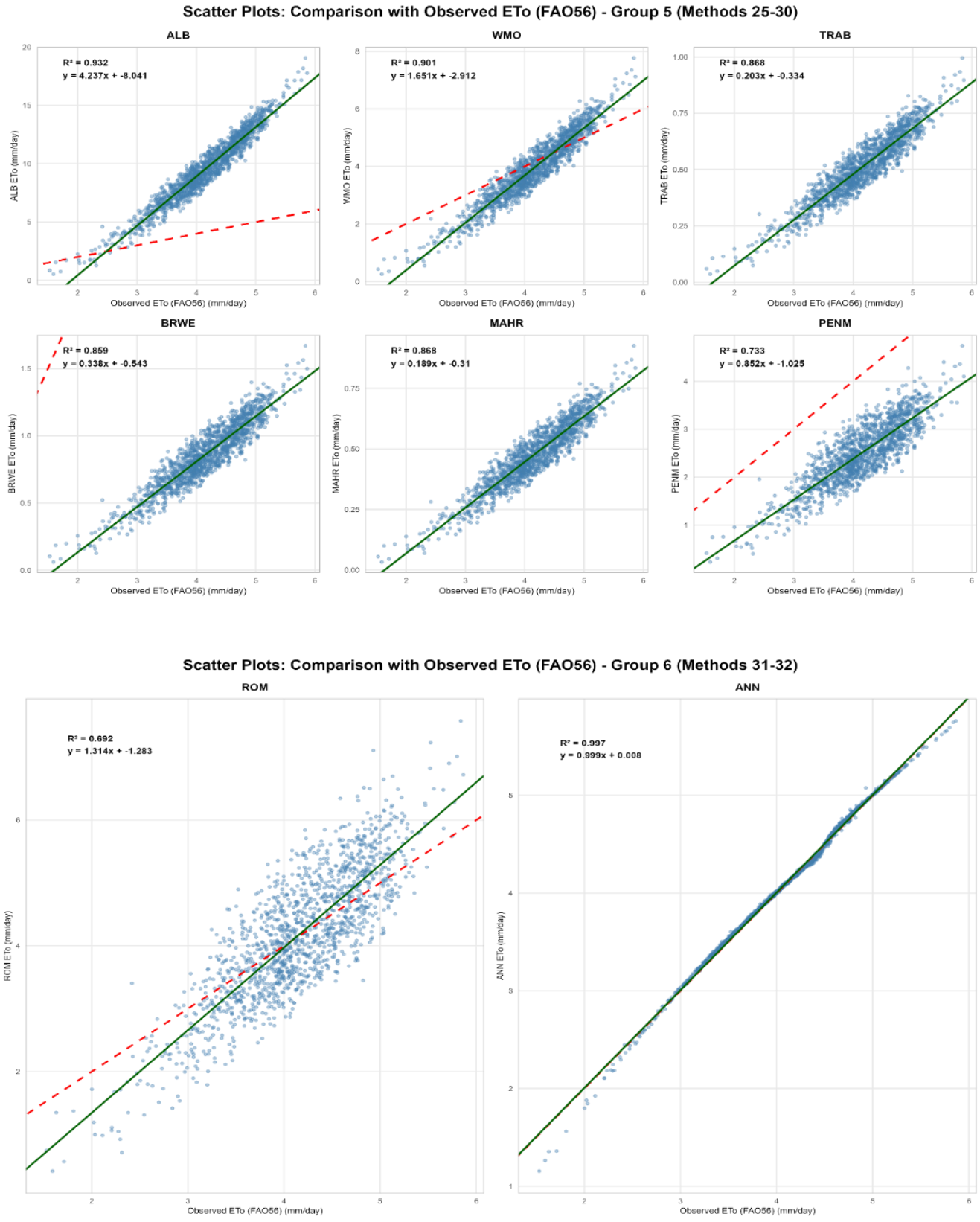

Figure 4. *Scatter plot diagrams of various methods for estimating ETo from 2019-2022.*

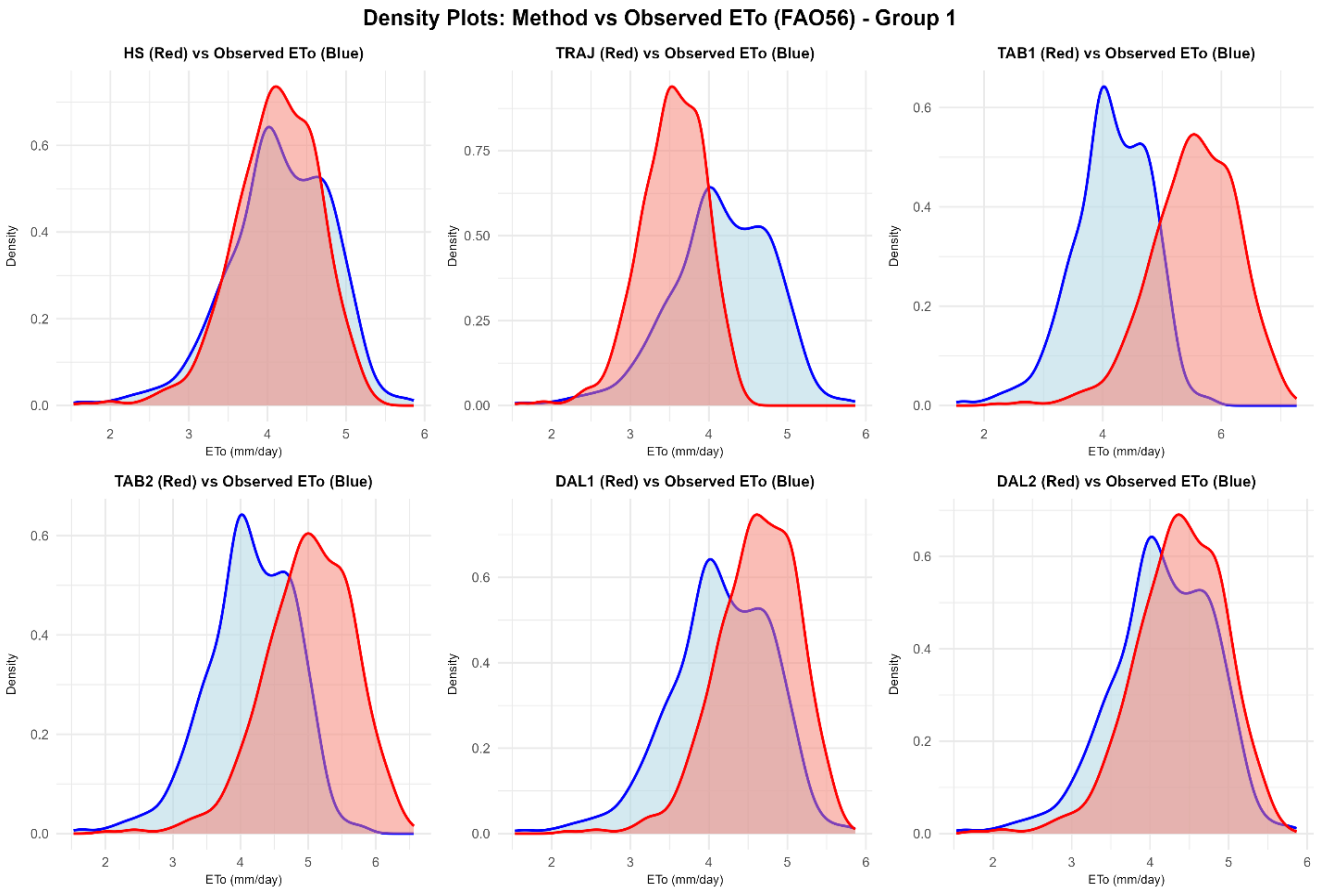
Density Plots: Method vs Observed ETo (FAO56) - Group 1
HS (Red) vs Observed ETo (Blue)
TRAJ (Red) vs Observed ETo (Blue)
TAB1 (Red) vs Observed ETo (Blue)
TAB2 (Red) vs Observed ETo (Blue)
DAL1 (Red) vs Observed ETo (Blue)
DAL2 (Red) vs Observed ETo (Blue)
Density
ETo (mm/day)

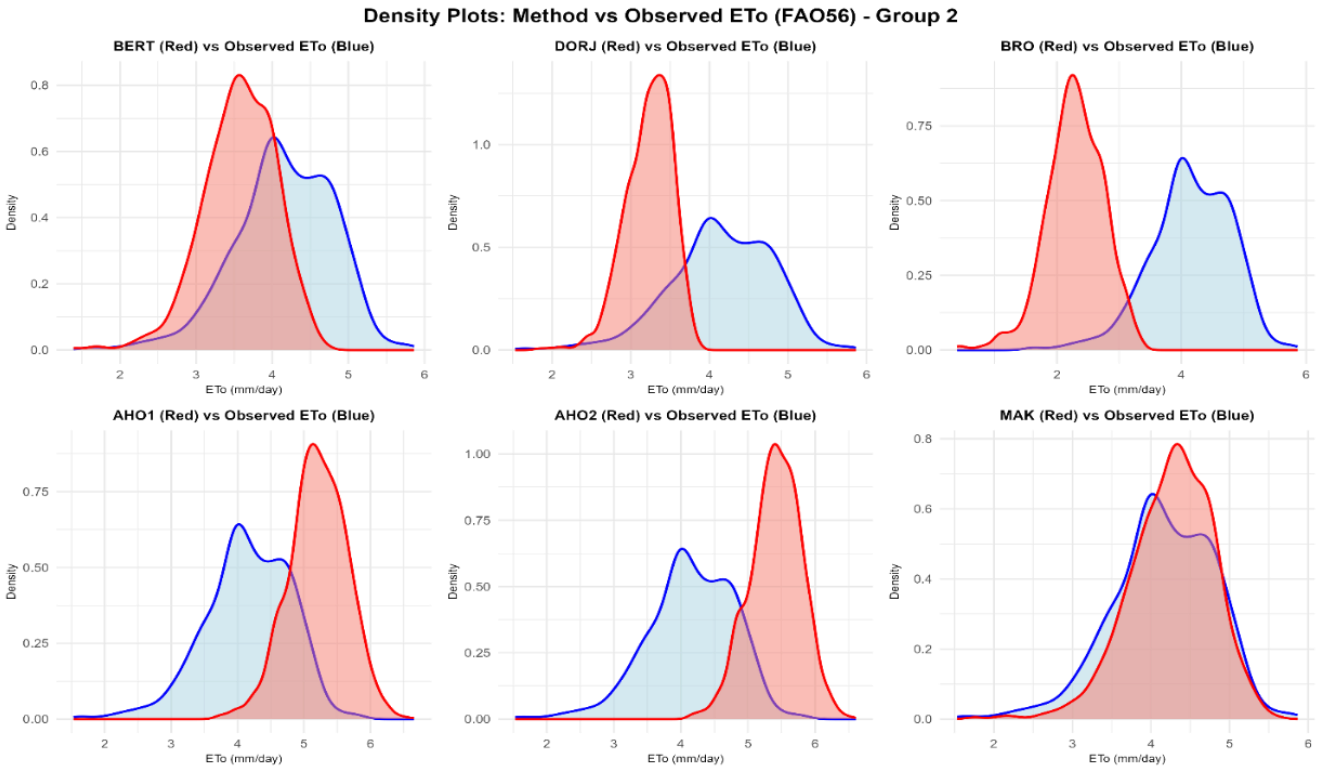
Density Plots: Method vs Observed ETo (FAO56) - Group 2
BERT (Red) vs Observed ETo (Blue)
DORJ (Red) vs Observed ETo (Blue)
BRO (Red) vs Observed ETo (Blue)
AHO1 (Red) vs Observed ETo (Blue)
AHO2 (Red) vs Observed ETo (Blue)
MAK (Red) vs Observed ETo (Blue)
Density
ETo (mm/day)

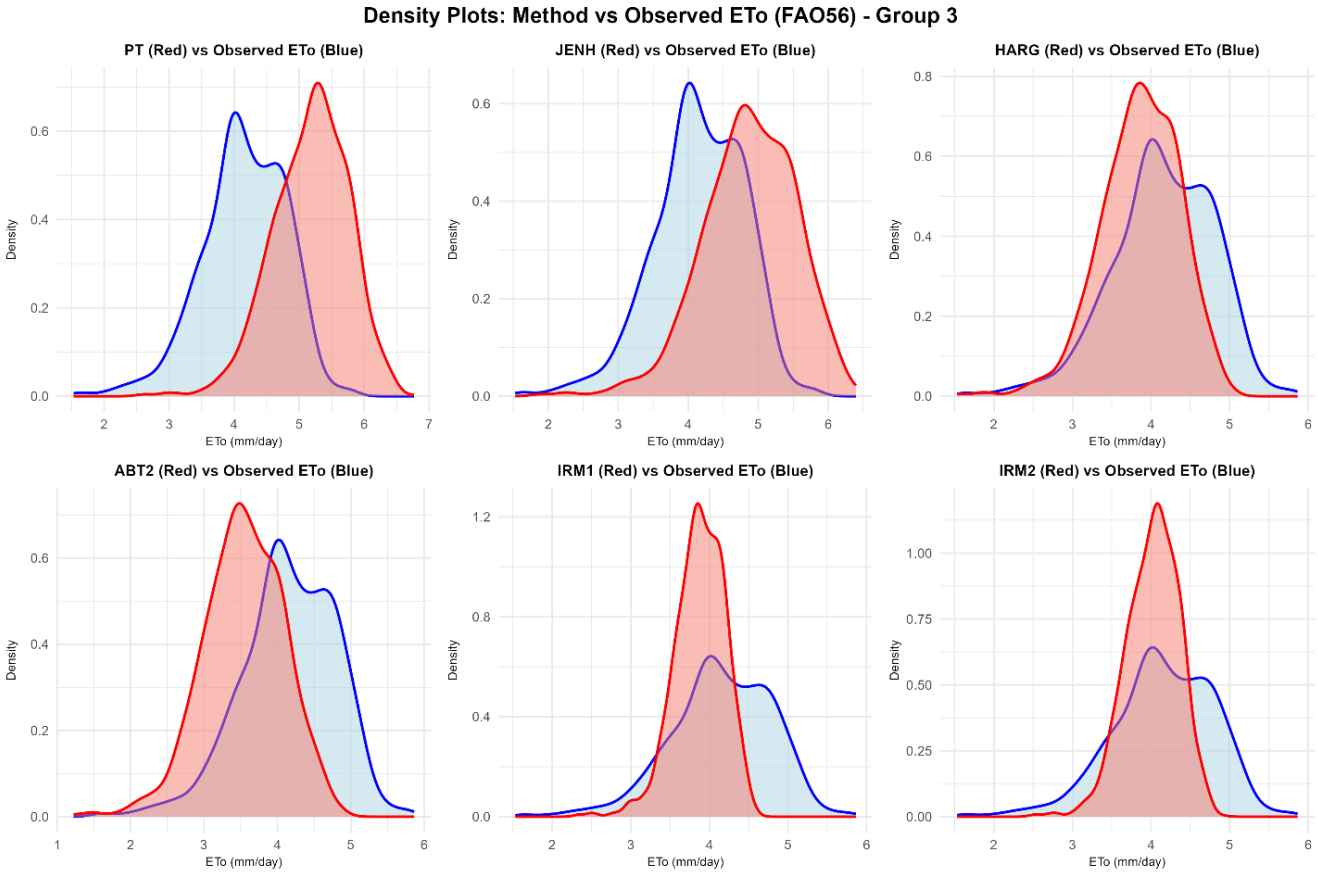
Density Plots: Method vs Observed ETo (FAO56) - Group 3
PT (Red) vs Observed ETo (Blue)
JENH (Red) vs Observed ETo (Blue)
HARG (Red) vs Observed ETo (Blue)
ABT2 (Red) vs Observed ETo (Blue)
IRM1 (Red) vs Observed ETo (Blue)
IRM2 (Red) vs Observed ETo (Blue)
Density
ETo (mm/day)

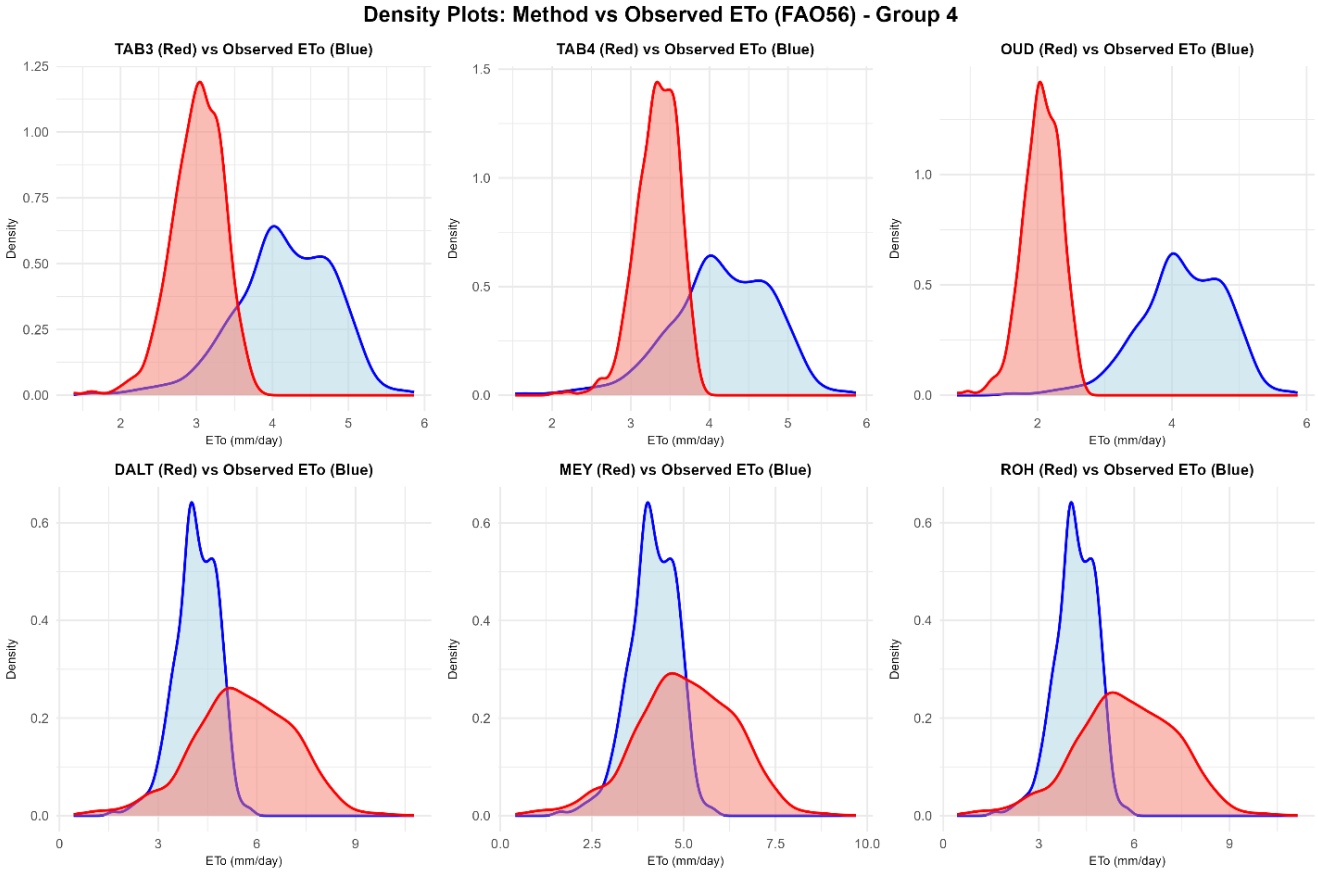
Density Plots: Method vs Observed ETo (FAO56) - Group 4
TAB3 (Red) vs Observed ETo (Blue)
TAB4 (Red) vs Observed ETo (Blue)
OUD (Red) vs Observed ETo (Blue)
DALT (Red) vs Observed ETo (Blue)
MEY (Red) vs Observed ETo (Blue)
ROH (Red) vs Observed ETo (Blue)
Density
ETo (mm/day)

Figure 5. *Density plots of the methods used to estimate ETo from 2019-2022.*

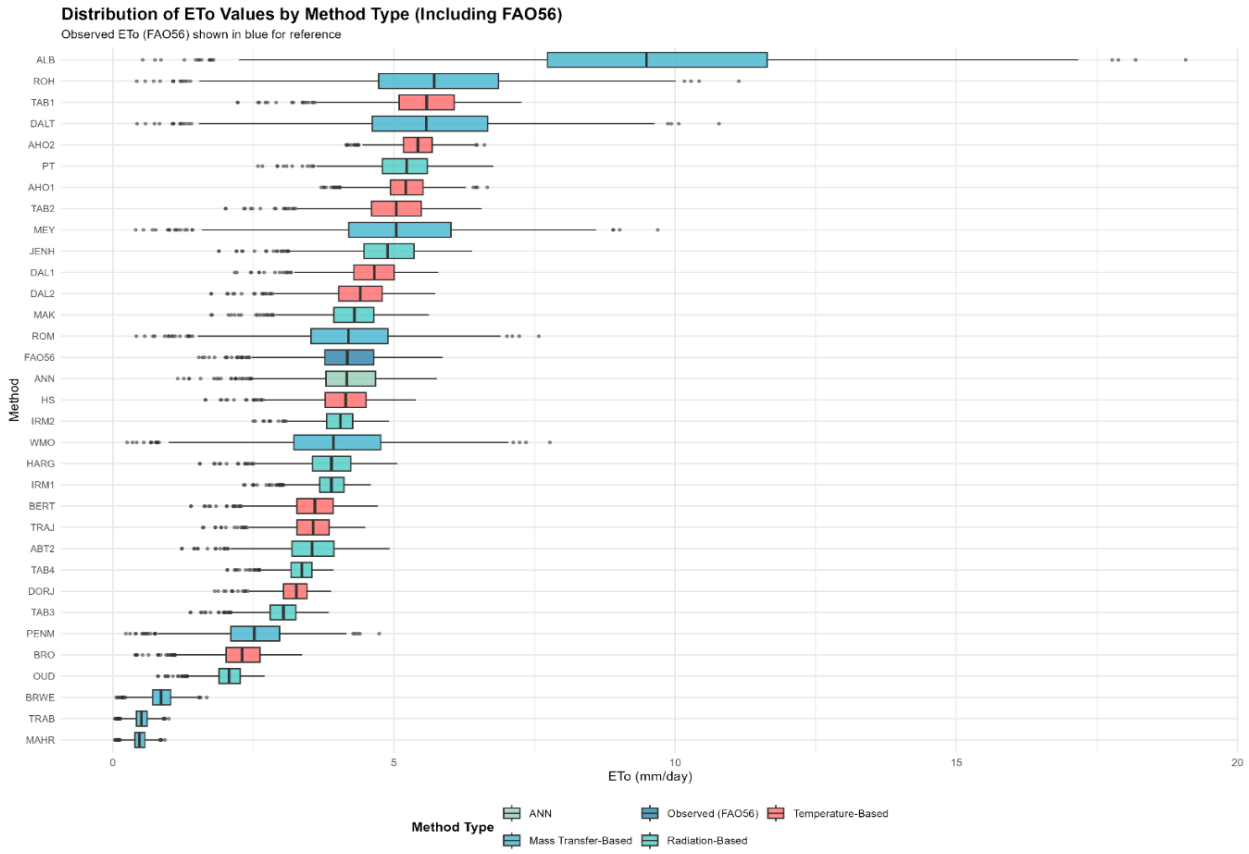

Figure 6. *Box plots of the methods used to estimate ETo from 2019-2022.*

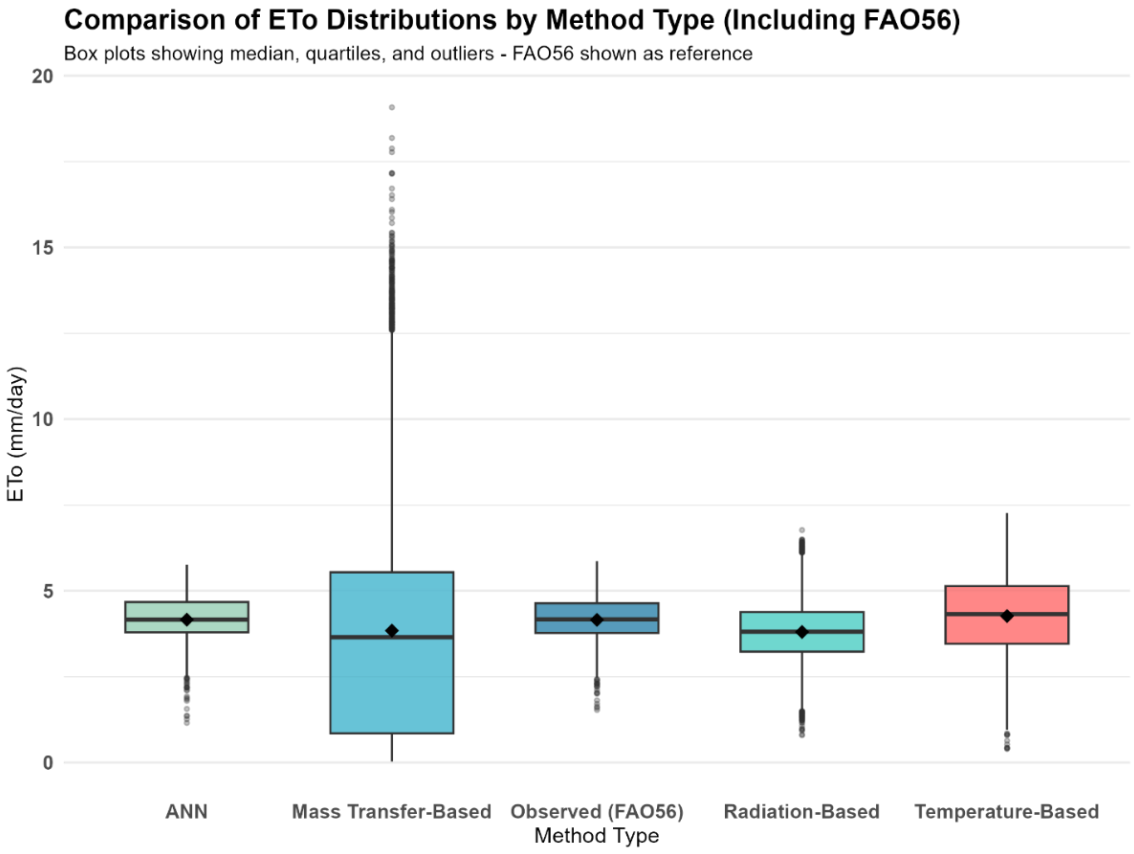

Figure 7. *Box plots by method type used for estimating ETo from 2019-2022.*

3.3. Performance Metric

The performance of 32 ETo estimation methods was evaluated against the FAO56 Penman-Monteith reference using eight statistical metrics: RMSE, MAE, MBE, MAPE, NRMSE, NSE, R^2, and loA. The complete performance metrics for all methods are presented in Table 5. Figure 8 presents RMSE values for the top 20 methods, while Figure 9 shows the R^2 and NSE comparisons for all methods, respectively. The proposed ANN model demonstrated exceptional performance across all metrics, achieving an RMSE of 0.0363 mm day $^{-1}$, MAE of 0.0256 mmday^{-1}, and a near-zero MBE of 0.0055 mm day-1 (Table 5; Figure 8). The NSE value of 0.9968 and R^2 of 0.9969 indicate near-perfect agreement with FAO56 (Table 5 and Figure 9), while the loA of 0.9992 confirms very good predictive accuracy, effectively matching the reference method.

Among temperature-based methods, the Hargreaves-Samani (HS) and Droogers and Allen-2 (DAL2) methods performed best, with RMSE values of 0.2958 and 0.3641 mm day^{-1}, respectively, and NSE values exceeding 0.68 (Table 5; Figure 9). In contrast, the Baier and Robertson (BRO) method performed worst (RMSE = 1.8877 mm day $^{-1}$, NSE = −7.522), while the Tabari and Talaee methods (TAB1, TAB2) exhibited systematic overestimation with positive MBE values exceeding 0.85 mm day^{-1} (Figure 10). Radiation-based methods showed considerable variation, with the Makkink (MAK) method performing best (RMSE = 0.3475 mm day^{-1}, NSE = 0.7111), while the Oudin (OUD) was the least performing method (RMSE = 2.1331 mm day^{-1}, NSE = −9.882). Mass transfer-based methods displayed the greatest variability, reflecting their historical development and sensitivity to wind speed inputs. The WMO method performed best within this category (RMSE = 0.5873 mm day^{-1}, R^2 = 0.9014), while the Albrecht (ALB) method performed worst overall (RMSE = 5.8453 mmday^{-1}, NSE = −80.714), confirming the limitations of purely aerodynamic approaches for ETo estimation (Table 5).

The scatter plots in Figures 11 and 12 provide a visual synthesis of method performance, clearly showing the ANN occupying the optimal quadrant of low RMSE with high R^2 and high NSE, while mass transfer methods cluster in the region of high RMSE and negative NSE values. The point sizes representing absolute bias (|MBE|) further highlight the ANN's minimal systematic error compared to the substantial biases exhibited by methods such as Albrecht and Oudin. These findings have important practical implications for Guyana: the ANN model's ability to replicate FAO56 accuracy with minimal input data requirements makes it particularly valuable for regions like Guyana, where full meteorological data are unavailable or limited. Among conventional approaches, the Hargreaves-Samani, Droogers, Allen-2, and Makkink methods offer reasonable alternatives when only temperature or radiation data are available, while mass transfer-based methods may not be appropriate for this region.

Table 5. *The performance metrics values of the different methods used.*

Method	RMSE	MAE	MBE	MAPE	NRMSE	NSE	R^2	IoA
HS	0.296	0.239	-0.040	5.850	7.120	0.791	0.798	0.935
TRAJ	0.698	0.623	-0.615	14.360	16.800	-0.164	0.807	0.714
TAB1	1.429	1.391	1.391	34.400	34.410	-3.885	0.798	0.527
TAB2	0.906	0.855	0.855	21.390	21.820	-0.964	0.798	0.683
DAL1	0.543	0.473	0.459	12.410	13.080	0.294	0.807	0.815
DAL2	0.364	0.303	0.220	7.790	8.770	0.683	0.799	0.911
BERT	0.659	0.587	-0.583	13.650	15.880	-0.040	0.796	0.749
DORJ	1.009	0.931	-0.924	21.530	24.300	-1.436	0.796	0.569
BRO	1.888	1.861	-1.861	45.090	45.440	-7.522	0.800	0.414
AHO1	1.107	1.057	1.057	27.380	26.650	-1.931	0.779	0.558
AHO2	1.303	1.256	1.256	32.540	31.370	-3.062	0.801	0.497
MAK	0.348	0.285	0.106	7.310	8.370	0.711	0.740	0.908
PT	1.089	1.023	1.022	26.070	26.220	-1.836	0.667	0.584
JENH	0.774	0.718	0.717	17.940	18.630	-0.433	0.814	0.742

Method	RMSE	MAE	MBE	MAPE	NRMSE	NSE	R^2	IoA
HARG	0.417	0.335	-0.290	7.770	10.030	0.585	0.798	0.875
ABT2	0.684	0.619	-0.618	14.670	16.470	-0.119	0.796	0.758
IRM1	0.472	0.383	-0.278	8.990	11.370	0.467	0.819	0.785
IRM2	0.432	0.345	-0.135	8.490	10.390	0.554	0.695	0.803
TAB3	1.206	1.144	-1.144	26.820	29.040	-2.479	0.781	0.528
TAB4	0.917	0.829	-0.815	19.020	22.080	-1.013	0.819	0.588
OUD	2.133	2.093	-2.093	50.090	51.350	-9.882	0.812	0.357
DALT	1.715	1.481	1.427	34.220	41.280	-6.033	0.839	0.568
MEY	1.202	0.991	0.890	23.070	28.930	-2.453	0.818	0.695
ROH	1.872	1.632	1.583	37.610	45.080	-7.385	0.856	0.538
ALB	5.845	5.418	5.407	125.330	140.720	-80.714	0.932	0.211
WMO	0.587	0.481	-0.208	12.650	14.140	0.175	0.901	0.890
TRAB	3.679	3.643	-3.643	87.920	88.580	-31.378	0.868	0.224
BRWE	3.323	3.294	-3.294	79.680	80.000	-25.413	0.859	0.250
MAHR	3.716	3.679	-3.679	88.770	89.460	-32.025	0.868	0.222
PENM	1.677	1.641	-1.641	40.240	40.380	-5.729	0.733	0.469
ROM	0.602	0.493	0.021	12.310	14.490	0.133	0.692	0.862
ANN	0.036	0.026	0.006	0.700	0.870	0.997	0.997	0.999

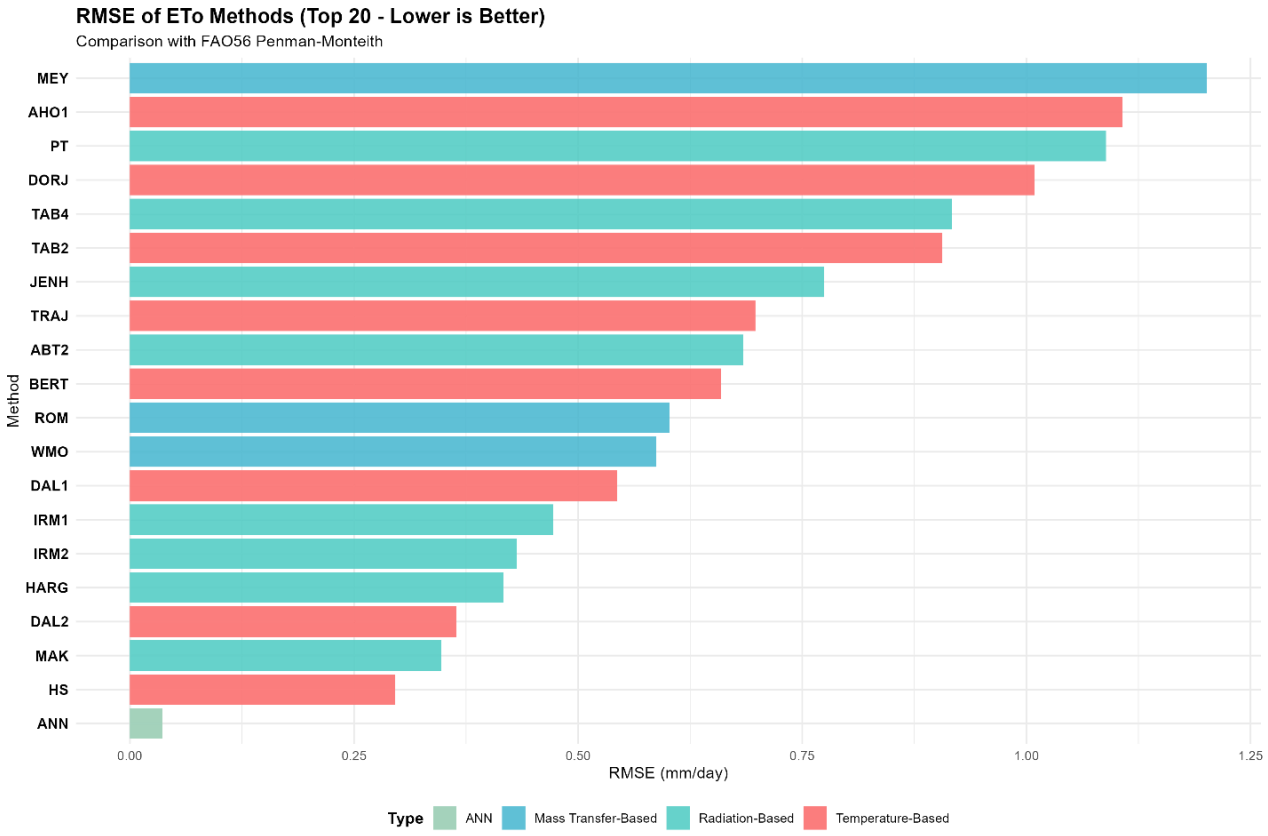

Figure 8. *Bar chart of the top 20 RSME for methods used.*

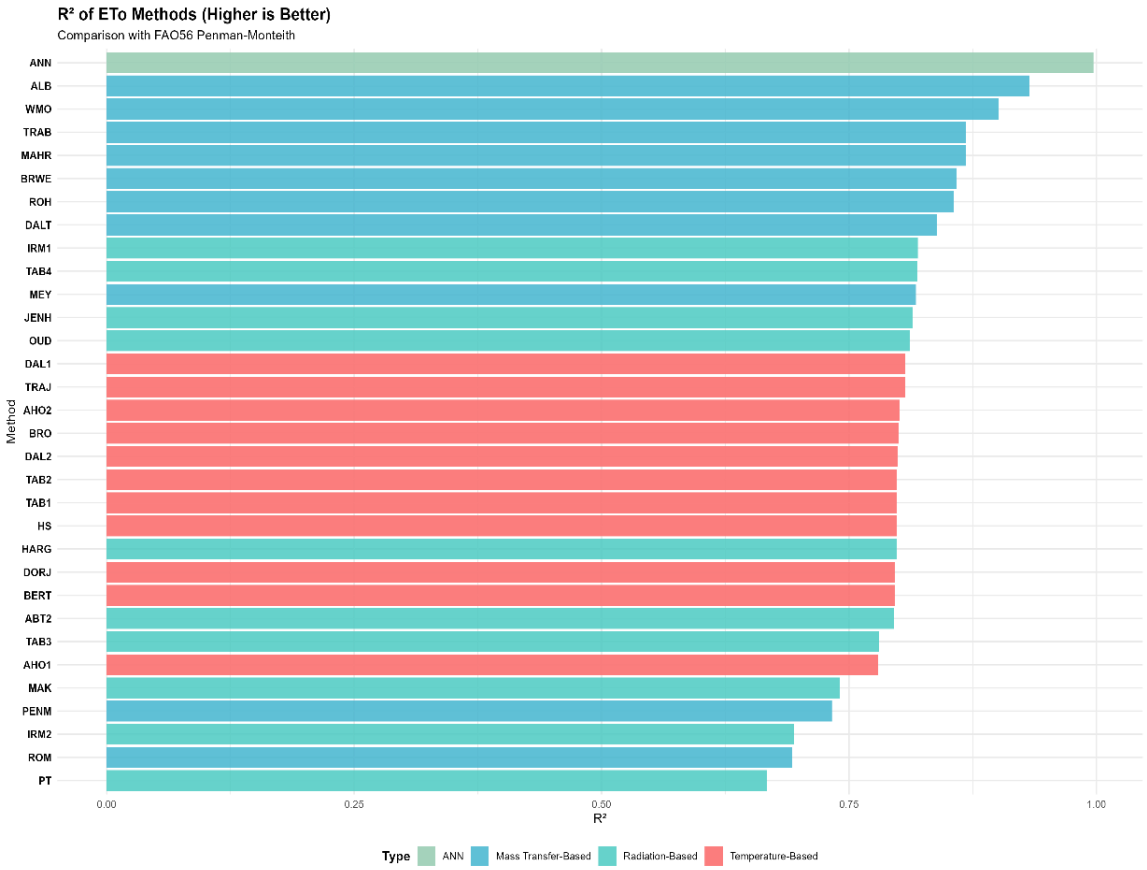

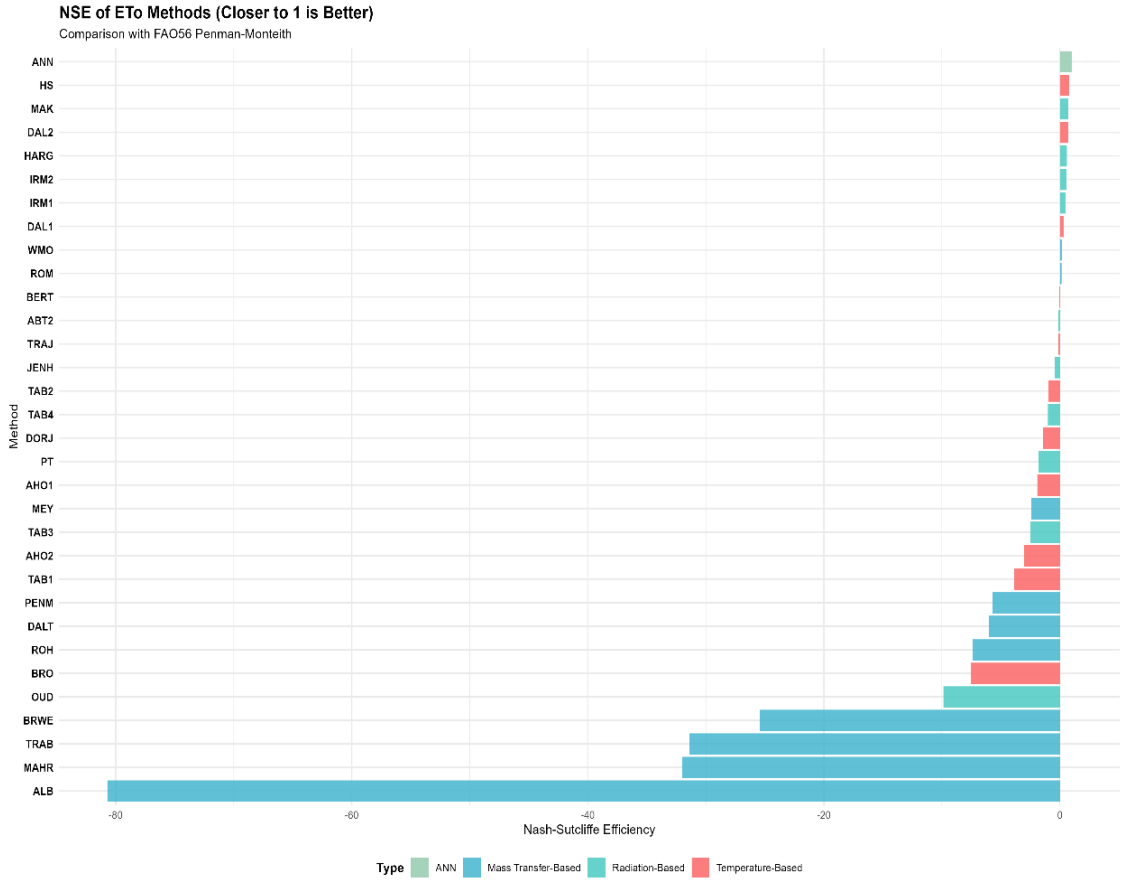

Figure 9. *Bar charts of R^2 and NSE for the various methods used to estimate ETo from 2019-2022.*

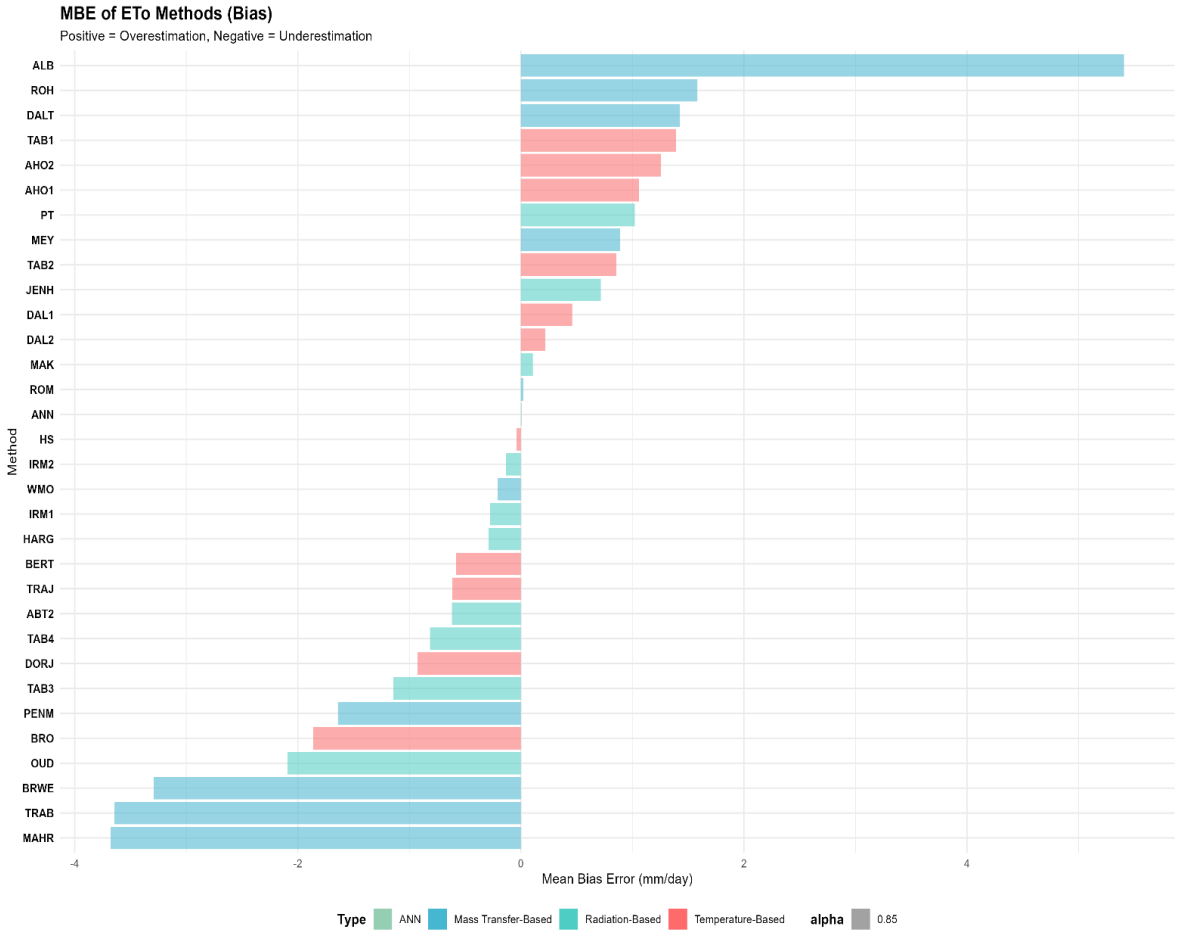

Figure 10. *Bar chart showing MBE of the methods used for estimating ETo from 2019-2022.*

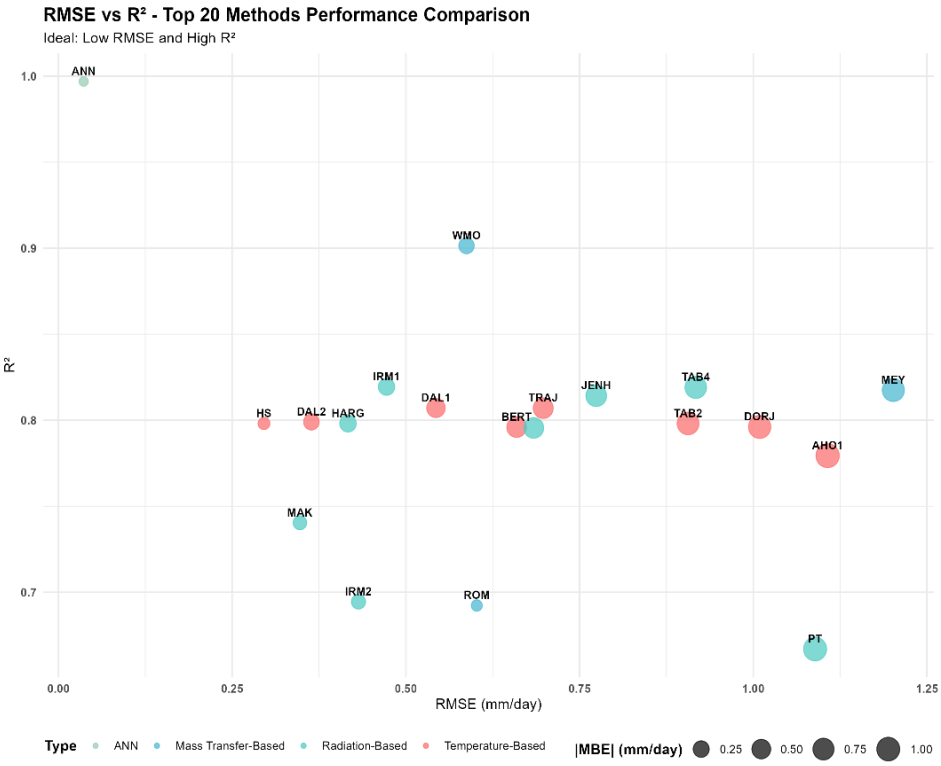

Figure 11. *Scatter plot diagram showing RMSE vs R^2 of the top 20 methods used.*

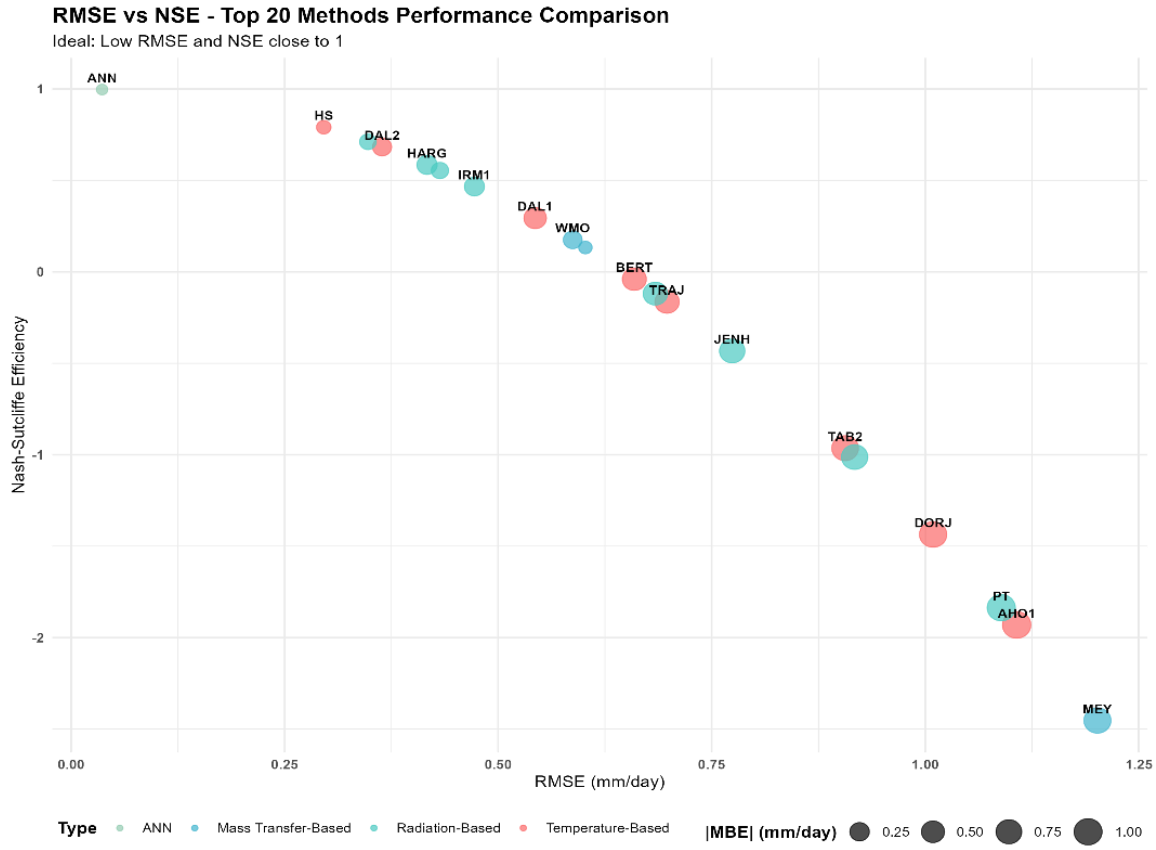

Figure 12. *Scatter plot diagram showing RMSE vs NSE of the top 20 methods used.*

4. Discussion

The results of this study demonstrate the effectiveness of using an artificial neural network (ANN) to estimate reference evapotranspiration (ETo) in Georgetown, Guyana, using observed meteorological inputs. The model, structured as (5–6–1) and trained on data from 2001 to 2018, showed exceptional generalisation capability when tested on unseen data from 2019 to 2022. Its performance was validated by several statistical metrics, all of which indicated strong predictive accuracy.

The close alignment between the descriptive statistics of the observed and predicted ETo values highlights the ANN model's ability to capture the underlying physical processes influencing evapotranspiration. The mean ETo values estimated by the ANN (4.159 mm/day) closely mirrored those computed via the FAO Penman-Monteith method (4.154 mm/day), with only negligible differences in standard deviation and distributional shape (as indicated by skewness and kurtosis). This similarity suggests that the ANN effectively learned the nonlinear relationships among the input climatic variables: maximum and minimum temperatures, relative humidity, solar radiation, and wind speed, that drive ETo variability.

A key contribution of this study lies in the comprehensive comparison of the ANN model with 32 empirical ETo estimation methods. While several temperature-based and radiation-based methods, such as [16, 24], showed moderate agreement with the FAO Penman–Monteith reference, their performance was consistently inferior to that of the ANN across all evaluation metrics. In contrast, mass transfer-based methods exhibited substantial variability and systematic bias, often producing extreme over- or underestimations, highlighting their limited applicability in such conditions where aerodynamic assumptions may not hold.

Moreover, the ANN model's low error rates, including a Root Mean Square Error (RMSE) of 0.036 mm/day and a Mean Absolute Error (MAE) of 0.026 mm/day, reflect its high level of precision. The near-zero Mean Bias Error (MBE = 0.006) further indicates minimal systematic over- or underestimation, while the low MAPE (0.700%) and Normalised RMSE (0.009) affirm the model's robustness and scalability. High efficiency and agreement indicators: NSE (0.997), R^2 (0.997), and IoA (0.999), further confirm that the ANN model explains almost all the variance in observed ETo and aligns very closely with the reference values.

These findings are consistent with previous research that reported strong ANN performance in ETo modelling across diverse climates and geographies [9, 12, 42].

Importantly, this study represents the first known application of ANN-based ETo modelling in the context of Guyana, where conventional methods like Penman-Monteith may be constrained by limited meteorological data. The successful

implementation of this ANN model demonstrates a viable alternative that can yield reliable ETo estimates using readily observed weather parameters. Such advancements are particularly valuable for improving water resource planning and agricultural productivity in data-scarce environments.

While the results are promising, future work could investigate hybrid models, integrate remotely sensed inputs, and integrate simulated weather data to further reduce data requirements or apply deep learning architectures to assess whether further accuracy gains can be achieved. Additionally, evaluating model performance across different seasons or rainfall regimes in Guyana could provide more granular insights into its applicability under varying climatic conditions.

5. Conclusions

This study successfully demonstrated the applicability of an artificial neural network (ANN) model for estimating reference evapotranspiration (ETo) in Georgetown, Guyana, using observed meteorological data. The model, trained with data from 2001 to 2018 and validated on independent observations from 2019 to 2022, showed excellent agreement with the FAO Penman-Monteith estimates. Performance metrics such as RMSE, MAE, NSE, R^2, and IoA confirmed the ANN model's high predictive accuracy and generalisation capacity.

In addition, when compared with 32 commonly used empirical ETo estimation methods, the ANN consistently outperformed all alternatives across the evaluated performance metrics, further reinforcing its reliability and robustness under humid tropical coastal conditions.

Given the challenges of acquiring complete climate datasets in developing countries, the ANN approach presents a practical and reliable alternative for ETo estimation. Its success in this study suggests that data-driven models can effectively support irrigation planning, agricultural decision-making, and water resource management in regions with similar data limitations.

Abbreviations

ANN	Artificial Neural Network
ETo	Reference Evapotranspiration
FAO	Food and Agriculture Organisation
ITCZ	Intertropical Convergence Zone
IoA	Index of Agreement
KNN	K-Nearest Neighbor
MAE	Mean Absolute Error
MAPE	Mean Absolute Percentage Error
MBE	Mean Bias Error
NRMSE	Normalised Root Mean Square Error
NSE	Nash-Sutcliffe Efficiency
PM	Penman–Monteith
R^2	Coefficient of Determination
ReLU	Rectified Linear Unit
RMSE	Root Mean Square Error
RMSprop	Root Mean Square Propagation

Author Contributions

Bunnel Bernard: Conceptualization, Investigation, Resources, Software, Visualization, Writing – original draft

Dwayne Shorlon Renville: Data curation, Methodology, Validation, Writing – review & editing

Linda Francois: Formal Analysis, Project administration, Software, Visualization

Data Availability Statement

The data is available from the corresponding author upon reasonable request.

Conflicts of Interest

The authors declare no conflicts of interest.

References

[1] F. Üneş, B. Taşar, Y. Z. Kaya, and M. Demirci, "The evaluation and comparison of daily reference evapotranspiration with ANN and empirical methods," International Journal of Engineering and Geosciences. 2018, vol. 3, no. 1, pp. 1–7. https://doi.org/10.26833/ijeg.331332

[2] R. G. Allen, M. Tasumi, A. Morse, and R. Trezza, "A Landsat-based energy balance and evapotranspiration model in Western US water rights regulation and planning," Irrigation and Drainage Systems. 2005, vol. 19, no. 3–4, pp. 251–268. https://doi.org/10.1007/s10795-005-5187-z

[3] F. H. S. Chiew, N. N. Kamaladasa, H. M. Malano, and T. A. McMahon, "Penman-Monteith, FAO-24 reference crop evapotranspiration and Class-A pan data in Australia," Agricultural Water Management. 1995, vol. 28, no. 1, pp. 9–21. https://doi.org/10.1016/0378-3774(95)01149-E

[4] J. M. Jacobs, S. Reddy, and J. M. Fitzgerald, Evaluation of reference evapotranspiration methodologies and AFSIRS crop water use simulation model. Final Report. Florida: Florida Department of Environmental Protection, 2001.

[5] B. Temesgen, S. Eching, B. Davidoff, and K. Frame, "Comparison of some reference evapotranspiration equations for California," Journal of Irrigation and Drainage Engineering. 2005, vol. 131, no. 1, pp. 73–84. https://doi.org/10.1061/(ASCE)0733-9437(2005)131:1(73)

[6] J. D. Valiantzas, "Simplified forms for the standardized FAO-56 Penman-Monteith reference evapotranspiration using limited weather data," Journal of Hydrology. 2013, vol. 505, pp. 13–23. https://doi.org/10.1016/j.jhydrol.2013.09.005

[7] J. Fan, W. Yue, L. Wu, F. Zhang, H. Cai, X. Wang, X. Lu, and Y. Xiang, "Evaluation of SVM, ELM and four tree-based ensemble models for predicting daily reference evapotranspiration using limited meteorological data in different climates of China," Agricultural and Forest Meteorology. 2018, vol. 263, pp. 225–241. https://doi.org/10.1016/j.agrformet.2018.08.019

[8] P. Lobit, A. Gómez Tagle, F. Bautista, and J. P. Lhomme, "Retrieving air humidity, global solar radiation, and reference evapotranspiration from daily temperatures: Development and validation of new methods for Mexico. Part III: Reference evapotranspiration," Theoretical and Applied Climatology. 2018, vol. 133, no. 3–4, pp. 787–797. https://doi.org/10.1007/s00704-017-2213-7

[9] M. Kumar, N. S. Raghuwanshi, R. Singh, W. W. Wallender, and W. O. Pruitt, "Estimating evapotranspiration using artificial neural network," Journal of Irrigation and Drainage Engineering. 2002, vol. 128, no. 4, pp. 224–233. https://doi.org/10.1061/(ASCE)0733-9437(2002)128:4(224)

[10] S. S. Zanetti, E. F. Sousa, V. P. S. Oliveira, F. T. Almeida, and S. Bernardo, "Estimating evapotranspiration using artificial neural network and minimum climatological data," https://doi.org/10.1061/ASCE0733-94372007133:283

[11] F. Parekh, "Estimating reference crop evapotranspiration using neural network fitting," International Journal of Computer Applications. 2014, vol. 93, no. 7, pp. 12–17. https://doi.org/10.5120/16130-5116

[12] V. Z. Antonopoulos and A. V. Antonopoulos, "Daily reference evapotranspiration estimates by artificial neural networks technique and empirical equations using limited input climate variables," Computers and Electronics in Agriculture. 2017, vol. 132, pp. 86–96. https://doi.org/10.1016/j.compag.2016.11.011

[13] S. O. Eastman and B. Khan, "Statistical analysis of rainfall data: A case study of Georgetown, Guyana," International Journal of Innovative Research in Multidisciplinary and Pedagogical Studies (IJIRMPS). 2022, vol. 10, no. 6. https://doi.org/10.37082/IJIRMPS.v10.i6.1612

[14] R. G. Allen, L. S. Pereira, M. Smith. Crop evapotranspiration: Guidelines for computing crop water requirements. Rome: Food and Agriculture Organization of the United Nations; 1998.

[15] J. S. Bojanowski, sirad: Functions for Calculating Daily Solar Radiation and Evapotranspiration. R package version 2.3-3. Available: http://sirad.r-forge.r-project.org/

[16] G. H. Hargreaves and Z. A. Samani, "Reference crop evapotranspiration from temperature," Applied Engineering in Agriculture. 1985, vol. 1, no. 2, pp. 96–99. https://doi.org/10.13031/2013.26773

[17] S. Trajković, "Hargreaves versus Penman–Monteith under humid conditions," Journal of Irrigation and Drainage Engineering. 2007, vol. 133, no. 1, pp. 38–42. https://doi.org/10.1061/(ASCE)0733-9437(2007)133:1(38)

[18] H. Tabari and P. Hosseinzadehtalaei, "Local calibration of the Hargreaves and Priestley–Taylor equations for estimating reference evapotranspiration in arid and cold climates of Iran based on the Penman–Monteith model," Journal of Hydrologic Engineering. 2011, vol. 16, no. 10, pp. 837–845. https://doi.org/10.1061/(ASCE)HE.1943-5584.0000366

[19] P. Droogers and R. G. Allen, "Estimating reference evapotranspiration under inaccurate data conditions," Irrigation and Drainage Systems. 2002, vol. 16, no. 1, pp. 33–45. https://doi.org/10.1023/A:1015508322413

[20] A. Berti, G. Tardivo, A. Chiaudani, F. Rech, and M. Borin, "Assessing reference evapotranspiration by the Hargreaves method in north-eastern Italy," Agricultural Water Management. 2014, vol. 140, pp. 20–25. https://doi.org/10.1016/j.agwat.2014.03.015

[21] U. Dorji, J. E. Olesen, and M. S. Seidenkrantz, "Water balance in the complex mountainous terrain of Bhutan and linkages to land use," Journal of Hydrology: Regional Studies. 2016, vol. 7, pp. 55–68. https://doi.org/10.1016/j.ejrh.2016.05.001

[22] W. Baier and G. W. Robertson, "Estimation of latent evaporation from simple weather observations," Canadian Journal of Plant Science. 1965, vol. 45, no. 3, pp. 276–284. https://doi.org/10.4141/cjps65-051

[23] M. Ahooghalandari, M. Khiadani, and M. E. Jahromi, "Developing equations for estimating reference evapotranspiration in Australia," Water Resources Management. 2016, vol. 30, pp. 3815–3828. https://doi.org/10.1007/s11269-016-1386-7

[24] G. F. Makkink, "Testing the Penman formula by means of lysimeters," Journal of the Institution of Water Engineers. 1957, vol. 11, pp. 277–288.

[25] C. H. B. Priestley and R. J. Taylor, "On the assessment of surface heat flux and evaporation using large-scale parameters," Monthly Weather Review. 1972, vol. 100, no. 2, pp. 81–92. https://doi.org/10.1175/1520-0493(1972)100%3C0081:OTAOSH%3E2.3.CO;2

[26] M. E. Jensen and H. R. Haise, "Estimating evapotranspiration from solar radiation," Journal of the Irrigation and Drainage Division. 1963, vol. 89, no. 4, pp. 15–41.

[27] G. H. Hargreaves, "Moisture availability and crop production," Transactions of the ASAE. 1975, vol. 18, no. 5, pp. 980–984. https://doi.org/10.13031/2013.36722

[28] W. Abtew, "Evapotranspiration measurements and modeling for three wetland systems in south Florida," Journal of the American Water Resources Association. 1996, vol. 32, no. 3, pp. 465–473. https://doi.org/10.1111/j.1752-1688.1996.tb04044.x

[29] S. Irmak, A. Irmak, R. G. Allen, and J. W. Jones, "Solar and net radiation-based equations to estimate reference evapotranspiration in humid climates," Journal of Irrigation and Drainage Engineering. 2003, vol. 129, no. 5, pp. 336–347. https://doi.org/10.1061/(ASCE)0733-9437(2003)129:5(336)

[30] L. Oudin, F. Hervieu, C. Michel, C. Perrin, V. Andréassian, F. Anctil, and C. Loumagne, "Which potential evapotranspiration input for a lumped rainfall–runoff model?" Journal of Hydrology. 2005, vol. 303, no. 1–4, pp. 290–306. https://doi.org/10.1016/j.jhydrol.2004.08.026

[31] J. Dalton, "Experimental essays, on the constitution of mixed gases; on the force of steam or vapour from water and other liquids in different temperatures, both in a Torricellian vacuum and in air; on evaporation; and on the expansion of gases by heat," Memoirs of the Literary and Philosophical Society of Manchester. 1798, vol. 5, no. 2, pp. 535–602. Available: https://www.biodiversitylibrary.org/part/308525

[32] A. Meyer, Über einige Zusammenhänge zwischen Klima und Boden in Europa. Zurich: ETH Zurich. 1926. https://doi.org/10.3929/ethz-a-000092038

[33] C. Rohwer and C. Rohwer, Evaporation from free water surfaces. https://doi.org/10.22004/AG.ECON.163103

[34] F. Albrecht, "Die Methoden zur Bestimmung der Verdunstung der natürlichen Erdoberfläche," Archiv für Meteorologie, Geophysik und Bioklimatologie, Serie B. 1950, vol. 2, no. 12, pp. 1–38.

[35] World Meteorological Organization Commission for Instruments and Methods of Observation, Measurement and estimation of evaporation and evapotranspiration. Geneva: Secretariat of the World Meteorological Organization, 1966.

[36] W. Trabert, "Neue Beobachtungen über Verdampfungsgeschwindigkeiten [New observations on evaporation rates]," Meteorologische Zeitschrift. 2007, pp. 261–263.

[37] B. Brockamp and H. Wenner, "Verdunstungsmessungen auf den Steiner See bei Münster," Deutsche Gewässerkundliche Mitteilungen. 1963, vol. 7, pp. 149–154.

[38] W. Mahringer, "Verdunstungsstudien am Neusiedler See," Archiv für Meteorologie, Geophysik und Bioklimatologie, Serie B. 1970, vol. 18, pp. 1–20. https://doi.org/10.1007/BF02245865

[39] H. L. Penman, "Natural evaporation from open water, bare soil and grass," Proceedings of the Royal Society A. 1948, vol. 193, no. 1032, pp. 120–145. https://doi.org/10.1098/rspa.1948.0037

[40] V. A. Romanenko, "Computation of the autumn soil moisture using a universal relationship for a large area," Proceedings of the Ukrainian Hydrometeorological Research Institute. 1961, vol. 3, pp. 12–25.

[41] S. K. Jain, P. C. Nayak, and K. P. Sudheer, "Models for estimating evapotranspiration using artificial neural networks, and their physical interpretation," Hydrological Processes. 2008, vol. 22, no. 13, pp. 2225–2234. https://doi.org/10.1002/hyp.6819

[42] K. G. Sheela and S. N. Deepa, "Review on methods to fix number of hidden neurons in neural networks," Mathematical Problems in Engineering. 2013. https://doi.org/10.1155/2013/425740

[43] S. Walls, A. D. Binns, J. Levison, and S. MacRitchie, "Prediction of actual evapotranspiration by artificial neural network models using data from a Bowen ratio energy balance station," Neural Computing and Applications. 2020, vol. 32, no. 17, pp. 14001–14018. https://doi.org/10.1007/s00521-020-04800-2

[44] G. Hinton, N. Srivastava, and K. Swersky, Neural Networks for Machine Learning: Lecture 6a Overview of Mini-Batch Gradient Descent. https://www.cs.toronto.edu/~tijmen/csc321/slides/lecture_slides_lec6.pdf

[45] W. B. Alves, G. D. S. Rolim, and L. E. D. O. Aparecido, "Reference evapotranspiration forecasting by artificial neural networks," Engenharia Agrícola. 2017, vol. 37, no. 6, pp. 1116–1125. https://doi.org/10.1590/1809-4430-eng.agric.v37n6p1116-1125/2017

[46] J. Maqsood, A. A. Farooque, F. Abbas, T. Esau, X. Wang, B. Acharya, and H. Afzaal, "Application of artificial neural networks to project reference evapotranspiration under climate change scenarios," Water Resources Management. 2022, vol. 36, no. 3, pp. 835–851. https://doi.org/10.1007/s11269-021-02997-y